A&A 632, A124 (2019)
https://doi.org/10.1051/0004-6361/201935544

Astronomy & Astrophysics

The MURALES survey

II. Presentation of MUSE observations of 20 3C low-*z* radio galaxies and first results

B. Balmaverde[1], A. Capetti[1], A. Marconi[2,3], G. Venturi[3,15], M. Chiaberge[4,5], R. D. Baldi[6], S. Baum[8,13], R. Gilli[7], P. Grandi[7], E. Meyer[11], G. Miley[9], C. O'Dea[8,12], W. Sparks[14], E. Torresi[7], and G. Tremblay[10]

[1] INAF – Osservatorio Astrofisico di Torino, Via Osservatorio 20, 10025 Pino Torinese, Italy
e-mail: balmaverde@oato.inaf.it
[2] Dipartimento di Fisica e Astronomia, Università di Firenze, Via G. Sansone 1, 50019 Sesto Fiorentino, Firenze, Italy
[3] INAF – Osservatorio Astrofisico di Arcetri, Largo Enrico Fermi 5, 50125 Firenze, Italy
[4] Space Telescope Science Institute, 3700 San Martin Dr., Baltimore, MD 21210, USA
[5] Johns Hopkins University, 3400 N. Charles Street, Baltimore, MD 21218, USA
[6] Department of Physics and Astronomy, University of Southampton, Highfield SO17 1BJ, UK
[7] INAF – Osservatorio di Astrofisica e Scienza dello Spazio di Bologna, via Gobetti 93/3, 40129 Bologna, Italy
[8] Department of Physics and Astronomy, University of Manitoba Winnipeg, MB R3T 2N2, Canada
[9] Leiden Observatory, Leiden University, PO Box 9513, 2300 RA Leiden, The Netherlands
[10] Harvard-Smithsonian Center for Astrophysics, 60 Garden St., Cambridge, MA 02138, USA
[11] University of Maryland Baltimore County, 1000 Hilltop Circle, Baltimore, MD 21250, USA
[12] School of Physics & Astronomy, Rochester Institute of Technology, Rochester, NY 14623, USA
[13] Carlson Center for Imaging Science, Rochester Institute of Technology, Rochester, NY 14623, USA
[14] SETI Institute, 189 N. Bernado Ave, Mountain View, CA 94043, USA
[15] Instituto de Astrofísica, Facultad de Física, Pontificia Universidad Católica de Chile, Casilla 306, Santiago 22, Chile

Received 26 March 2019 / Accepted 3 October 2019

ABSTRACT

We present observations of a complete sub-sample of 20 radio galaxies from the Third Cambridge Catalog (3C) with redshift <0.3 obtained from VLT/MUSE optical integral field spectrograph. These data have been obtained as part of the survey MURALES (a MUse RAdio Loud Emission line Snapshot survey) with the main goal of exploring the active galactic nuclei (AGN) feedback process in a sizeable sample of the most powerful radio sources at low redshift. We present the data analysis and, for each source, the resulting emission line images and the 2D gas velocity field. Thanks to their unprecedented depth (the median 3σ surface brightness limit in the emission line maps is 6×10^{-18} erg s^{-1} cm^{-2} arcsec^{-2}), these observations reveal emission line structures extending to several tens of kiloparsec in most objects. In nine sources the gas velocity shows ordered rotation, but in the other cases it is highly complex. 3C sources show a connection between radio morphology and emission line properties. Whereas, in three of the four Fanaroff and Riley Class I radio galaxies (FR Is), the line emission regions are compact, ∼1 kpc in size; in all but one of the Class II radiogalaxies FR IIs, we detected large scale structures of ionized gas with a median extent of 17 kpc. Among the FR IIs, those of high and low excitation show extended gas structures with similar morphological properties, suggesting that they both inhabit regions characterized by a rich gaseous environment on kpc scale.

Key words. galaxies: active – galaxies: ISM – galaxies: nuclei – galaxies: jets

1. Introduction

Radio galaxies are among the most energetic manifestations of active galactic nuclei and harbor the most massive black holes (SMBHs) in the Universe, typically hosted in the brightest galaxies at center of clusters or groups. They are therefore extraordinarily relevant to address important unknowns related to the interaction between SMBHs and their environment (Gitti et al. 2012). Significant progress in understanding the fueling and evolution of the activity of radio loud active galactic nuclei (AGNs), the triggering process of the radio emission, and its impact on the environment, has been made by studying the third Cambridge catalog of radio galaxies (3C, Spinrad et al. 1985). The 3C is the premiere statistically complete sample of powerful radio galaxies; it includes variety of extended radio morphologies, optical classes, and environmental properties.

The study of radio-loud AGN has become particularly important due to their role in the so-called feedback process, that is the exchange of matter and energy between AGN, their host galaxies, and clusters of galaxies. The evidence of kinetic AGN feedback mode is often witnessed in local radiogalaxies, showing the presence of cavities inflated by the radio emitting gas in the X-ray images. However, little is known about the coupling between radio-jets and ionized gas, whether the jets are able to accelerate the gas above the host escape velocity (McNamara & Nulsen 2007), and we also lack clear observational evidence on whether jets enhance or quench star formation (positive or negative feedback, e.g., Fabian 2012). Furthermore, the mechanical luminosity released by the AGN is not well-constrained because the cavity expansion speed is estimated using indirect and model-dependent approaches. Finally, the radiative output from the AGN can produce fast outflows

of ionized gas, which also affect the properties of the ambient medium (e.g., Wylezalek & Zakamska 2016; Carniani et al. 2016; Cresci & Maiolino 2018).

A study of the optical-line-emitting gas properties in low redshift radio galaxies (mostly from the 3C) has been performed by Baum et al. (1988), Baum & Heckman (1989), and extended to higher redshift by McCarthy et al. (1995). The analysis of narrow band images centered on the Hα +[N II] or [O III] emission lines, reveals that extended optical-line-emitting gas is common in powerful radio galaxies. The ionized gas is often distributed along filamentary structures on scales of 40–100 kpc, which eventually connect the host radio galaxy to possible companions. Baum et al. (1988) noted that the extended emission-line gas is preferentially observed along the radio source axis: this suggests that the distribution and/or the ionization of this gas is influenced by the radio source. It has also been suggested that tidal interactions and mergers could be related to the formation of a radio jet, since many radio galaxies show morphological and/or kinematic evidences for a recent encounter. However, no firm conclusion can be drawn about the origin of the extended optical line emitting gas: it can not be excluded that the emission line gas has cooled out from the hot intergalactic medium or that it has an internal origin (i.e., a merger has stirred up and redistributed the gas that was already present in the host galaxy before the interaction).

To investigate the mechanism of ionization in the extended emitting gas regions, Baum et al. (1990, 1992) used diagnostic diagrams (BPT diagrams, Baldwin et al. 1981; Veilleux & Osterbrock 1987) based on emission line ratios. They found line-ratio changes within individual sources along the elongated structures, but much higher variations from source to source, suggesting different ionization mechanisms. Separating the objects according to their kinematical properties in rotators, calm non rotators and violent rotators, they found that in rotators (mostly FR II, Fanaroff & Riley 1974) the forbidden lines (as [N II], [S II], [O I]) appear to be weak compared to Hα. This indicates that photoionization from the nuclear continuum is the dominant ionization mechanism. Instead, in calm non rotators (mostly FR I) they usually observed high [N II] to Hα ratios, which they interpreted to be produced by heating from cosmic rays. Other models can not be ruled out, such as clouds that condense out of the hot (10^7 K) gas and are ionized by soft X-ray photons, or gas with super-solar abundances, photoionized by the AGN.

The emission line regions in radio galaxies have also been extensively studied with the *Hubble* Space Telescope (HST). The Wide Field Planetary Camera-2 images of 80 3CR radio sources up to $z = 1.4$ (Privon et al. 2008) show that the radio and optical emission-line structures present a weak alignment at low redshift (z <0.6), which becomes stronger at higher redshift. They found a trend for the emission-line nebulae to be larger and more luminous with increasing redshift and/or radio power. Baldi et al. (2019) present Advanced Camera for Surveys emission line images of 19 low z 3C radio galaxies. They generally show extended [O III] emission, a large [O III]/Hα scatter across the galaxies, and a radio-line alignment effect. The line morphologies of high and low excitation galaxies (HEG and LEG, respectively, Hine & Longair 1979) are different; the former is brighter and more extended.

Integral field spectroscopic data provide us with a unique opportunity to study of the impact of AGN feedback in galaxies, mapping the distribution and the kinematics of the ionized gas with respect to the radio jet. Couto et al. (2017) observed the radio galaxy 3C 033 with GEMINI-GMOS/IFU (over a field of view of 4×6 kpc^2) revealing complex motions, with signatures of inflow and outflows. In NGC 3393, a nearby Seyfert 2 galaxy with nuclear radio jets and a nuclear bar, Finlez et al. (2018) with the same spectrograph found motions of rotation and outflows, traced by narrow emission line and broad component along the radio lobes and perpendicularly to them. With respect to these studies, the wider MUSE field of view ($1' \times 1'$) allows us to trace the distribution of the ionized emitting gas at distances of ~110–270 kpc (at $z = 0.1$ and 0.3, respectively), exploring the effect of AGN feedback at different spatial scales.

The physical processes that distribute the feedback energy of the AGN shaping the intracluster medium is a subject of intense theoretical efforts. Up to date cosmological hydrodynamic simulation of a galaxy cluster succeed in matching observations (Tremmel et al. 2019). However, the micro-physical processes that distribute the feedback energy remain uncertain and a subject of intense theoretical efforts. Multi wavelength observations have started to unveil the complex multi-phase structure of early-type elliptical galaxies (ETGs) at the center of groups and clusters. In optical, extended Hα and [N II] filaments up to 10 kpc from the center, are tightly correlated with soft X-ray and cold molecular gas (McDonald et al. 2010; Russell et al. 2019). Theoretical models predict that, at least in cool core clusters, cold clouds can condense out of a hot, turbulent and rarefied atmosphere and rain down to the black hole (Gaspari et al. 2017; Voit et al. 2015).

We have started MURALES (MUse RAdio Loud Emission lines Snapshot) project, a program aimed at observing the 3C radio sources with the integral field spectrograph MUSE at the VLT (Bacon et al. 2010). Our main goals are to study the feedback process in a sample of the most powerful radio sources at low redshift, to constrain the coupling between the radio source and the warm gas, to probe the fueling process, and to estimate the net effect of the feedback on star formation.

The MUSE data will enable us to (1) obtain deep line emission images and to compare them with the X-ray structures, exploring the spatial link between the hot and warm ionized ISM phases, and with the radio outflows, (2) derive spatially resolved emission lines ratios maps and explore the gas physical conditions, (3) map and characterize the full 2D ionized gas velocity field, (4) obtain the 2D stellar velocity field that will be compared with that observed in the gaseous component, (5) detect star forming regions, in search of positive feedback with young stars form along the jets path and/or around the radio lobes.

An example of the capabilities of MUSE comes from the observations of 3C 317, a radio-galaxy located at the center of the Abell cluster A2052 (Balmaverde et al. 2018a). A complex network of emission lines filaments enshrouds the whole northern cavity. The ionized gas kinematics show the hallmarks of a shell expansion, with both blue- and red-shifted regions, with a velocity of ~250 km s^{-1} (a factor of ~2 lower than previous indirect estimates based on X-ray data) leading to an estimate of the cavity age of 1.1×10^7 years. We did not detect any star-forming regions from the emission line ratios.

With the MUSE observations we also found a dual AGN associated to 3C 459 (Balmaverde et al. 2018b) whose host shows the signatures of a recent merger, i.e., disturbed morphology and a young stellar population. The line emission images show two peaks separated by ~4 kpc with radically different line profiles and ratios, and a velocity offset of ~300 km s^{-1}. The secondary AGN has properties typical of a highly obscured QSO, heavily buried at the center of the merging galaxies, producing a high ionization bicone extending more than 70 kpc.

Here we present the results of the observations of the first 20 3C sources obtained in Period 99. The paper is organized as follows: in Sect. 2 we present the sample observed, provide an

Table 1. Main properties of 3C sub sample observed with MUSE and observations log.

Name	z	FR	Class	L_{178} [erg s^{-1} Hz^{-1}]	L.A.S radio [kpc]	r [kpc]	Obs. date	Seeing [″]	Weather	Depth
3C 015	0.073	I	LEG	33.30	70	1.5	Jun. 30 2017	0.65	TN	5.6
3C 017	0.220	II	BLO	34.44	54	14.9	Jul. 20 2017	0.49	TN/CL	5.9
3C 018	0.188	II	BLO	34.27	178	24.8	Jun. 30 2017	0.53	TN	5.9
3C 029	0.045	I	LEG	32.84	125	0.9	Jul. 20 2017	0.51	TN/CL	3.2
3C 033	0.060	II	HEG	33.65	288	11.2	Jun. 30 2017	0.63	TN	7.4
3C 040	0.018	I	LEG	32.29	440	1.2	Jul. 22 2017	0.40	TN/CL.	7.5
3C 063	0.175	II	HEG	34.21	56	38.0	Jul. 21 2017	0.49	TN	7.5
3C 318.1	0.045	–	–	32.72			Jun. 22 2017	1.38	CL	6.3
3C 327	0.105	II	HEG	33.98	469	19.5	Jun. 30 2017	0.70	TN	6.3
3C 348	0.155	I	ELEG	35.35	153	34.0	Jul. 20 2017	1.76	CL	3.5
3C 353	0.030	II	LEG	33.69	111	17.2	Jun. 29 2017	1.30	CL	4.1
3C 386	0.017	II	–	32.18	77	11.1	Jun. 03 2017	0.61	TN	7.3
3C 403	0.059	II	HEG	33.16	101	8.3	Jun. 30 2017	0.54	TN	5.5
3C 403.1	0.055	II	LEG	32.98	236	5.6	Jun. 30 2017	0.80	TN	4.5
3C 424	0.127	II	LEG	33.78	28	32.9	Jul. 01 2017	0.98	TN	1.2
3C 442	0.026	II	LEG	32.39	286	3.8	Jun. 30 2017	0.61	TN	11.3
3C 445	0.056	II	BLO	33.26	483	18.5	Jul. 01 2017	1.48	TN/CL	5.2
3C 456	0.233	II	HEG	34.23	24		Jun. 30 2017	1.27	TN	8.8
3C 458	0.289	II	HEG	34.58	943	111.3	Jul. 22 2017	0.50	TN/CL	5.6
3C 459	0.220	II	BLO	34.55	31	76.0	Jul. 22 2017	0.43	TN/CL	19.3

Notes. Column description: (1) source name; (2) redshift; (3) and (4) FR and excitation class; (5) radio luminosity at 178 MHz from Spinrad et al. (1985); (6) largest angular size of the radio source; (7) largest distance of emission line detection in kpc units; (8) date of the observation; (9) mean seeing in the V band at zenith during the observation; (10) sky conditions during the observations: (TN) thin cirrus clouds (CL) clear night; (11) surface brightness limit of emission lines at 3σ in units of 10^{-18} erg s^{-1} cm^{-2} arcsec^{-2}.

observation log, and describe the data reduction. In Sect. 3 we present the resulting emission line images, line ratio maps, and 2D velocity fields. We also provide a description of the individual sources. In Sect. 4 we study the spectra of the extended emission line regions. The results are discussed in Sect. 5 and summarized in Sect. 6.

We adopt the following set of cosmological parameters: $H_o = 69.7$ km s^{-1} Mpc^{-1} and $\Omega_m = 0.286$ (Bennett et al. 2014).

2. Observation and data reduction

We observed a sample of 20 radio galaxies with MUSE as part of the MURALES survey. The sample is formed by all the 3C radio-sources limited to $z < 0.3$ and $\delta < 20°$, visible during the April-September semester, i.e., RA $< 3^h$ and RA $> 15^h$. Their main properties are listed in Table 1. They are in the redshift range $0.018 < z < 0.289$, with 11 sources located at $z < 0.1$. Their radio power spans more than two orders of magnitude, from $\sim 10^{24}$ to $\sim 2 \times 10^{26}$ W Hz^{-1} at 178 MHz. Most of them (15) are FR II. All optical spectroscopic classes (LEGs, HEGs, and broad lined objects, BLOs) are represented with an almost equal share of LEGs (including four FR II/LEGs) and HEGs/BLOs. We compare the redshift and radio power distribution of our sample with that of the entire population of 114 3C radio galaxies at $z < 0.3$ presented by Buttiglione et al. (2009). The mean redshift and radio power are $z = 0.11$ and $\log L_{178} = 33.58$ erg s^{-1}, respectively, not dissimilar from the values measured for the entire 3C sub-sample with $z < 0.3$ ($z = 0.13$ and $\log L_{178} = 33.61$ erg s^{-1}). The Kolmogorov–Smirnov test confirms that the two distributions of z and L_{178} are not statistically distinguishable. Our sub-sample can then be considered as well representative of the population of powerful, low redshift, radio galaxies.

The observations were obtained as part of the program ID 099.B-0137(A). Two exposures of 10 min each (except for 3C 015 and 3C 348 for which the exposure times were 2×13 and 2×14 min, respectively) were obtained with the VLT/MUSE spectrograph between June 3rd, 2017, and July 22nd, 2017 covering the wavelength range 4800–9300 Å. The median seeing of the observations is 0.″65. We split the total exposure time on source in two sub-exposures, applying a small dithering pattern and a 90 degrees rotation between on-object exposures to reject cosmic rays. A negligible cross-pattern remains in the final image, due to the observations with the two position angles of 0 and 90 degree. We used the ESO MUSE pipeline (version 1.6.2) with default settings to obtain fully reduced and calibrated data cubes. In detail, the pipeline applies the standard reduction procedure, i.e. corrects for the bias, the dark, the flat, the vignetting, removes cosmic rays and calibrates each exposure in wavelength and in flux. In each pixel a sky background model is subtracted and a sigma clipping method is implemented to remove cosmic rays from individual exposures. For the flux calibration, the pipeline uses a pre-processed spectro-photometric standard star observation, taken during clear or photometric nights, selected to be the closest to the expected position of the reference source. A known issue of the MUSE calibration procedure is that the sky subtraction is currently not optimal and the astrometry in some cases not precise, failing the identification of the stars depending on the observing conditions.We used the position of bright sources in the MUSE field observed by Pan-STARRS survey (Chambers et al. 2016) to correct for astrometric offset. More details about the reduction strategy are described in the MUSE Pipeline User Manual[1].

[1] ftp://ftp.eso.org/pub/dfs/pipelines/muse/muse-pipeline-manual-2.4.1.pdf

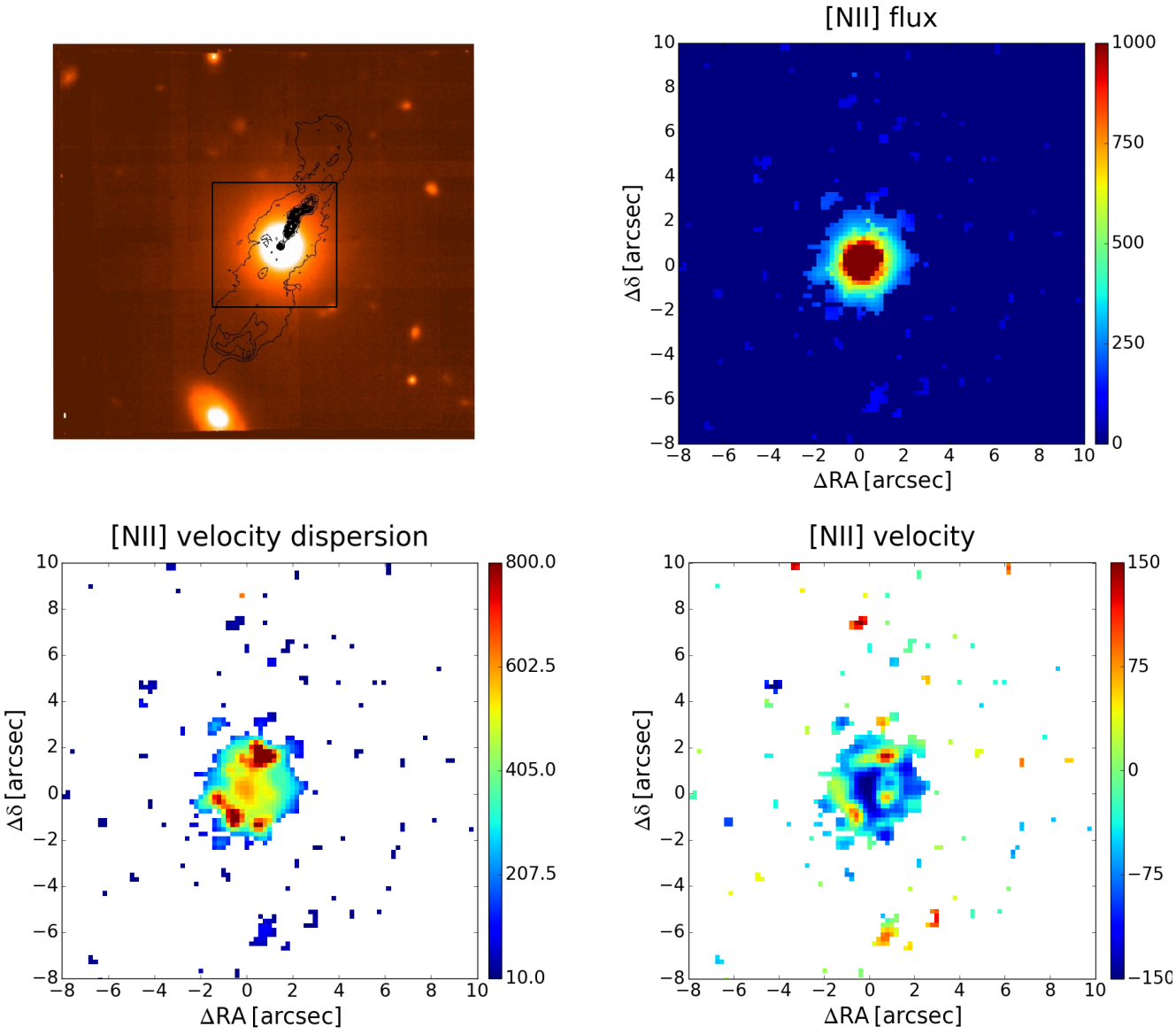

Fig. 1. 3C 015, FR I/LEG, 1″ = 1.40 kpc. *Top left*: radio contours (black) overlaid onto the Muse optical continuum image in the 5800 and 6250 Å rest frame range. The size of the image is the whole MUSE field of view, 1′ × 1′. *Top right*: [N II] emission line image extracted from the black square marked in the *left panel*. Surface brightness is in 10^{-18} erg s^{-1} cm^{-2} arcsec^{-2}. *Bottom*: velocity field and velocity dispersion for the [N II] line. Velocities are in km s^{-1} units.

We followed the same strategy for the data analysis described in Balmaverde et al. (2018b). Summarizing, we resampled the data cube with the Voronoi adaptive spatial binning (Cappellari & Copin 2003), requiring an average signal-to-noise ratio on the continuum per wavelength channel of at least 50. We then used Penalized Pixel-Fitting code (Cappellari 2017) to fit the stellar continuum and absorption features, which we finally subtracted from each spaxel in the data cube. Over most of the field-of-view, well outside of the host galaxies, the continuum emission is actually negligible and the spectra are completely dominated by emission lines. This procedure, that nonetheless we applied to all spaxels, often does not have any effect on the data.

We simultaneously fit all emission lines in the blue (namely H$\beta\lambda$4863, [O III]$\lambda\lambda$4960,5008) and in the red ([O I]$\lambda\lambda$6302, 6366, [N II]$\lambda\lambda$6550,6685, H$\alpha\lambda$6565, [S II]$\lambda\lambda$6718,6733) portion of the spectrum in the continuum subtracted spectra in each spaxel. We assumed that all lines in the blue and red portion of the spectra have the same profile. For the broad lined objects (BLO) we allowed for the presence of a broad component in the Balmer lines on the nucleus.

A single Gaussian component usually reproduces accurately the line profiles. However, for some objects, we had to include additional components in the central regions.

3. Results

We here focus on the properties of the ionized gas as probed by various emission lines. The results of the analysis are presented in Figs. 1–B.11. For each source we derived a continuum image (integrating the rest-frame line-free region between 5800 and 6250 Å) on which we superposed the radio contours from radio maps, retrieved from the NRAO VLA Archive Survey. In many cases the size of the radio source exceeds the whole MUSE field of view and, in most objects, the size of the region where emission lines are detected. For this reason we did not overlay the radio contours onto the emission line images. We also

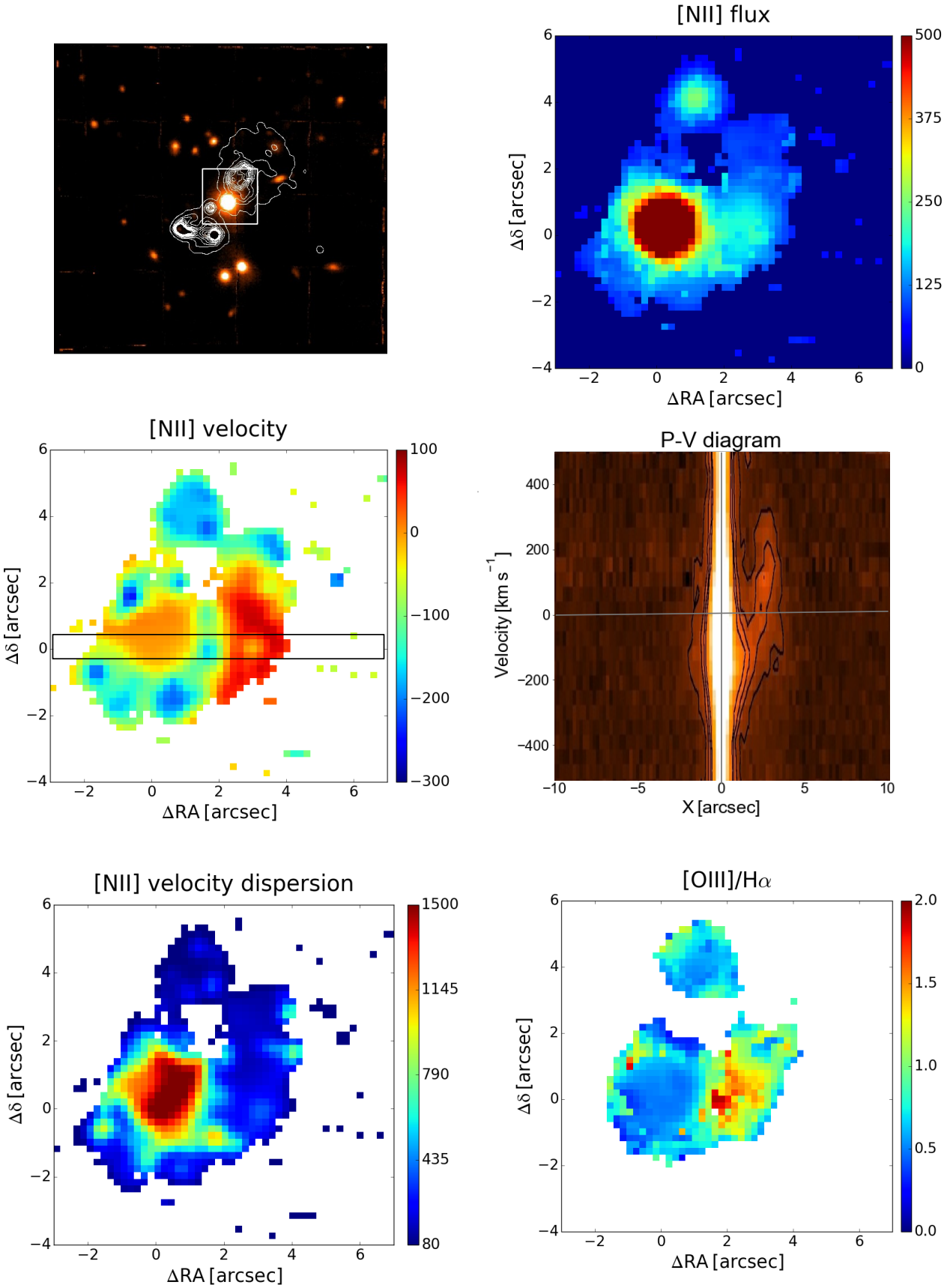

Fig. 2. 3C 017, FR II/BLO, 1″ = 3.58 kpc. *Top left*: radio contours (in white) overlaid onto the Muse optical continuum image over the MUSE field of view. *Top right*: [N II] emission line image extracted from the white square marked in the *left panel*. *Middle left*: gas velocity obtained from the [N II] line. *Middle right*: position-velocity diagram extracted from the synthetic slit shown overlaid onto the velocity field. *Bottom*: velocity dispersion and [N II] map of the [O III]/Hα line ratio. Surface brightness is in 10^{-18} erg s^{-1} cm^{-2} arcsec^{-2}, velocities are in km s^{-1} units.

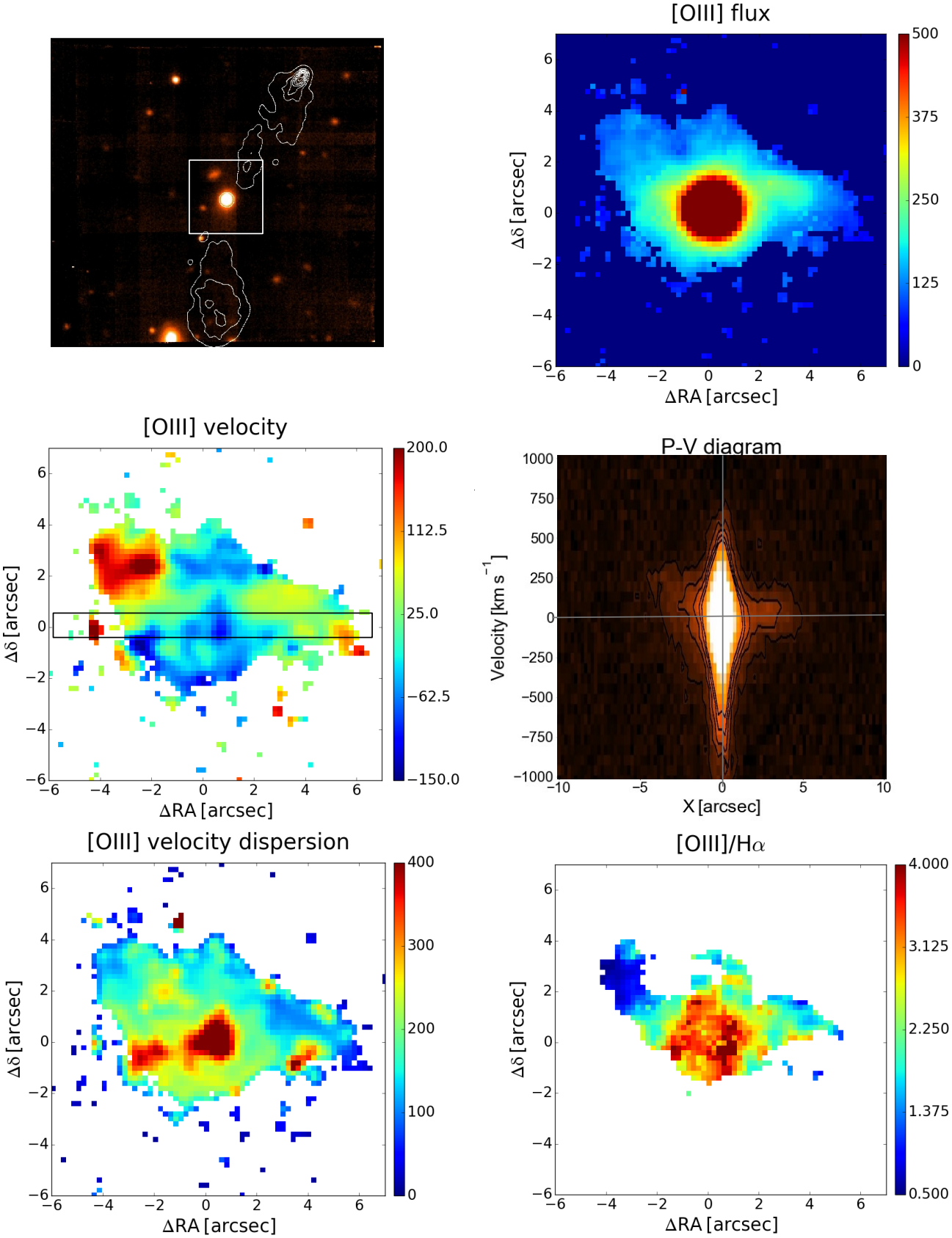

Fig. 3. 3C 018, FR II/BLO, 1″ = 3.17 kpc. *Top*: radio contours overlaid onto the Muse optical continuum image and [O III] emission line image extracted from the white square in the *top left panel*. *Middle*: velocity field from the [O III] line and position-velocity diagram extracted from the synthetic slit shown overlaid onto the velocity field (represented by the region centered on the nucleus, has a width of 5 pixels and oriented at an angle of 0° measured from the X axis). *Bottom*: velocity dispersion and [O III]/Hα ratio.

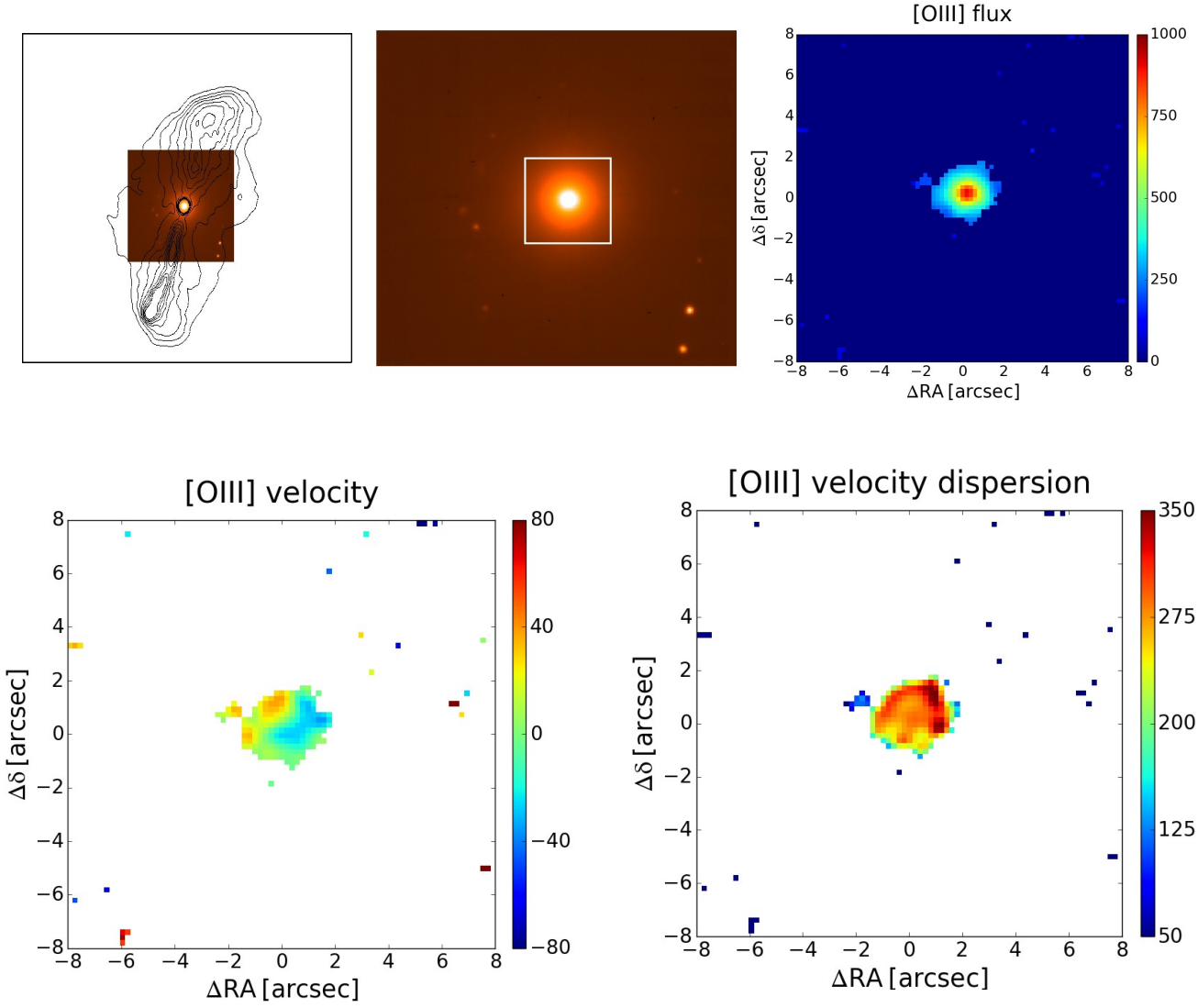

Fig. 4. 3C 029, FR I/LEG, 1″ = 0.89 kpc. *Top left*: radio contours overlaid onto the Muse optical continuum image. *Top center*: Muse optical continuum image. *Top right*: [O III] emission line image extracted from the white square in the *top center panel*. *Bottom*: velocity field from the [O III] line and velocity dispersion. Surface brightness is in 10^{-18} erg s^{-1} cm^{-2} arcsec^{-2}, velocities are in km s^{-1} units.

produced images in the different emission lines and obtained the correspondent gas velocity field. The velocity map are referred to the recession velocity derived from redshift. When necessary, we add a velocity shift to set the velocity in the nuclear region equal to zero. In the figures we show the intensity of the brightest line, usually the [N II] or [O III]. When the line emission is resolved we present the 2D gas velocity maps and the position-velocity diagram extracted along a synthetic long-slit aperture aligned with interesting line structures. This is possible for all sources except 3C 015, 3C 029, and 3C 456. All maps are centered at the position of the peak in the optical continuum images obtained from the MUSE datacube over a wavelength range free of emission lines. We show only spaxels with a signal to noise ratio (S/N) larger than 2. North is up and East is left; angles are all measured counterclockwise. In the following we describe the results obtained for the individual sources.

We here present the main results for the individual sources. In Figs. 1–B.11 we show the continuum image with superposed the radio contours, the image of the brightest emission lines and the corresponding velocity field and velocity dispersion. We also produced a position-velocity diagram along the direction of largest line extent for all well resolved line emission regions as well as a ratio image between the brightest line ([O III] or [N II]) and Hα. In the Appendix we present the nuclear spectra of all sources extracted from a single pixel at the continuum peak and the spectra of the 14 sources for which we explore the ionization properties of the extended emission line regions (see Fig. A.1).

3C 015. FR I/LEG, 1″ = 1.40 kpc. The emission lines are only slightly extended and confined within the central ∼3″ (∼4 kpc). The compactness of this source prevents us from producing a well resolved gas velocity field. The velocity dispersion is larger along the radio axis, reaching ≳800 km s^{-1}.

3C 017. FR II/BLO, 1″ = 3.58 kpc. Beside the bright central nuclear component, characterized by the presence of broad Balmer lines, the ionized gas extends in the NW direction out to ∼15 kpc. The gas velocity increases moving to the West up to ∼100 km s^{-1}, but when turning toward the North it decreases to blueshifted velocities, down to ∼−200 km s^{-1}. In addition, a blueshifted compact emission line knot is found ∼20 kpc to the North. The velocity dispersion is, except on the nucleus, rather

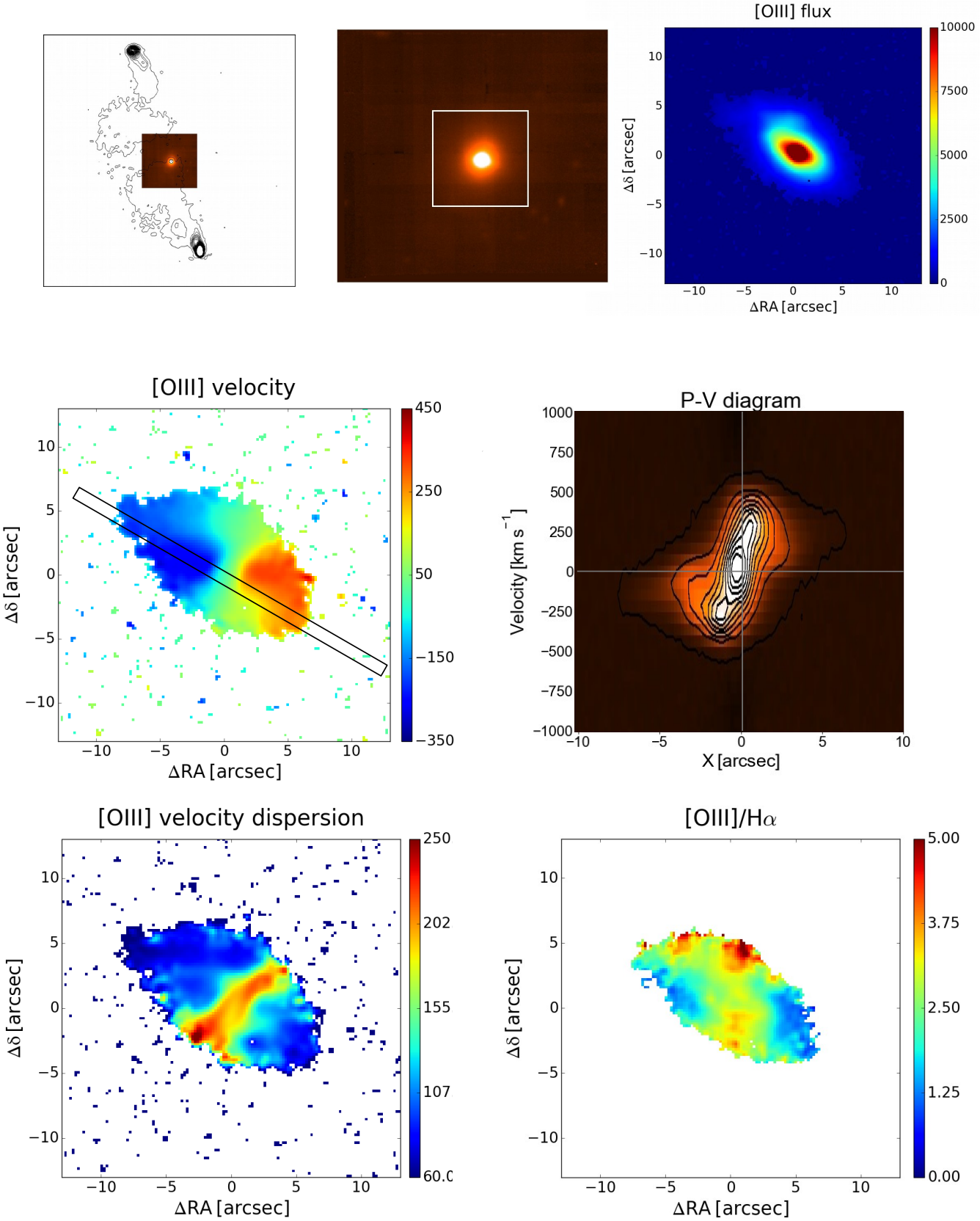

Fig. 5. 3C 033, FR II/HEG, 1″ = 1.17 kpc. *Top left*: radio contours overlaid onto the Muse optical continuum image. *Top center*: Muse optical continuum image. *Top right*: [O III] emission line image extracted from the white square in the *top center panel*. *Middle*: velocity field from the [O III] line and position-velocity diagram extracted from the synthetic slit shown overlaid onto the velocity field (the slit is centered on the nucleus, has a width of 5 pixels and it is oriented at an angle of −60° from the X axis.). *Bottom*: velocity dispersion and [O III]/Hα ratio.

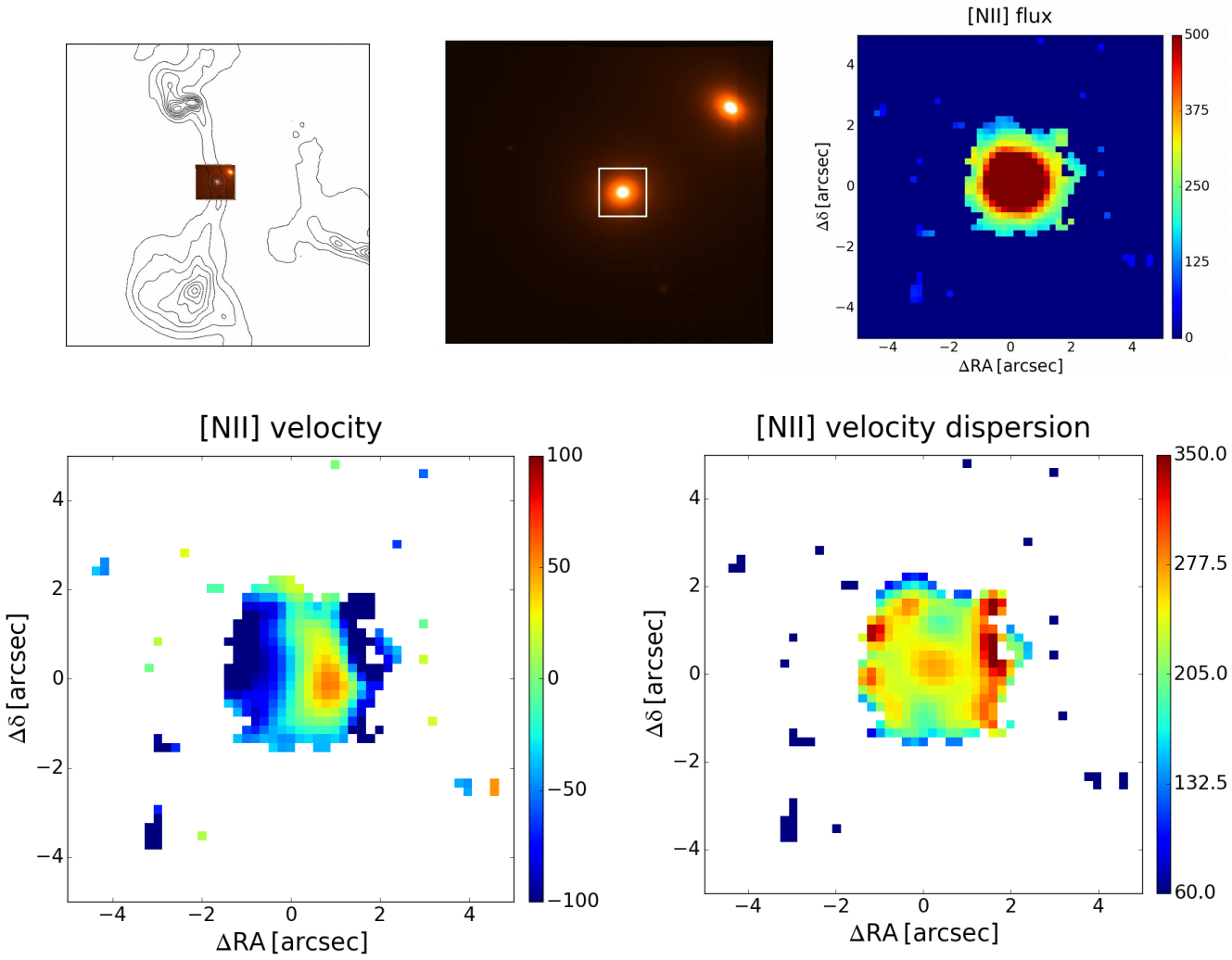

Fig. 6. 3C 040, FR I/LEG, 1″ = 0.37 kpc. *Top left*: radio contours overlaid onto the Muse optical continuum image. *Top center*: Muse optical continuum image. *Top right*: [N II] emission line image extracted from the white square in the *top center panel*. *Bottom*: velocity field from the [N II] line and [N II] velocity dispersion.

small. The [O III]/Hα line ratio in the west region is enhanced by a factor ∼3 compared to the nucleus.

3C 018. FR II/BLO, 1″ = 3.17 kpc. Diffuse line emission, elongated in the EW direction, surrounds the broad lined nucleus out to ∼15 kpc. The lines are redshifted on both sides of the nucleus, by ∼200 km s^{-1} on the West and by ∼100 km s^{-1} on the East where they are slightly blue-shifted in the perpendicular N–S direction. The velocity dispersion is always much larger than the instrumental width, with typical values of ∼200 km s^{-1}. The [O III]/Hα ratio decreases the nucleus toward the extended regions, from ∼4 to ∼0.5.

3C 029. FR I/LEG, 1″ = 0.89 kpc. Similarly to 3C 015, the line emission is only marginally extended. There is a hint of rotation along a line of nodes oriented at ∼120°.

3C 033. FR II/HEG, 1″ = 1.17 kpc. The MUSE field-of-view covers only ∼1/4 of the extension of the radio source. The ionized gas has an elliptical shape, extending out to ∼8″ (∼9 kpc) on both sides of the nucleus, and elongated along PA ∼ 50°, then twisting along PA ∼ 70°. The velocity field is broadly dominated by ordered rotation, with a line of nodes initially at PA ∼ 75°, then twisting at smaller angles. Outside the central regions of high velocity gradient, the most distant gas shows a constant rotation of ∼300 km s^{-1}. The velocity dispersion is enhanced along a linear region parallel to the line of nodes. The [O III]/Hα ratio is smaller in the west and east regions, and larger in a region approximately aligned with the radio axis, suggestive of a ionization cone.

3C 040. FR I/LEG, 1″ = 0.37 kpc. This source shows a FR I morphology, with diffuse radio plumes (not fully shown in Fig. 6) extending by more than ∼20′. Emission lines are detected in a compact but resolved region extending by ∼3″ (∼1 kpc). Gas rotation is detected, around PA ∼ 75°, with an amplitude of ∼300 km s^{-1}.

3C 063. FR II/HEG, 1″ = 2.99 kpc. The size of the emission line region is similar to that of this double-lobed radio source. On the east side the gas extends along PA ∼ 80° for ∼8″ (∼25 kpc) with a small velocity gradient. On the opposite side, emission lines extend initially toward the South-West, out to ∼10″, well aligned with the radio axis. At the location of the southern hot spot, the gas sharply bend toward the North, forming an arc-like structure, located at a distance of ∼33 kpc from the nucleus, wrapping around the southern lobe. This feature is dominated by a series of compact knots, surrounding the outer edge of the radio lobe. The gas velocity initially has a positive gradient, reaching

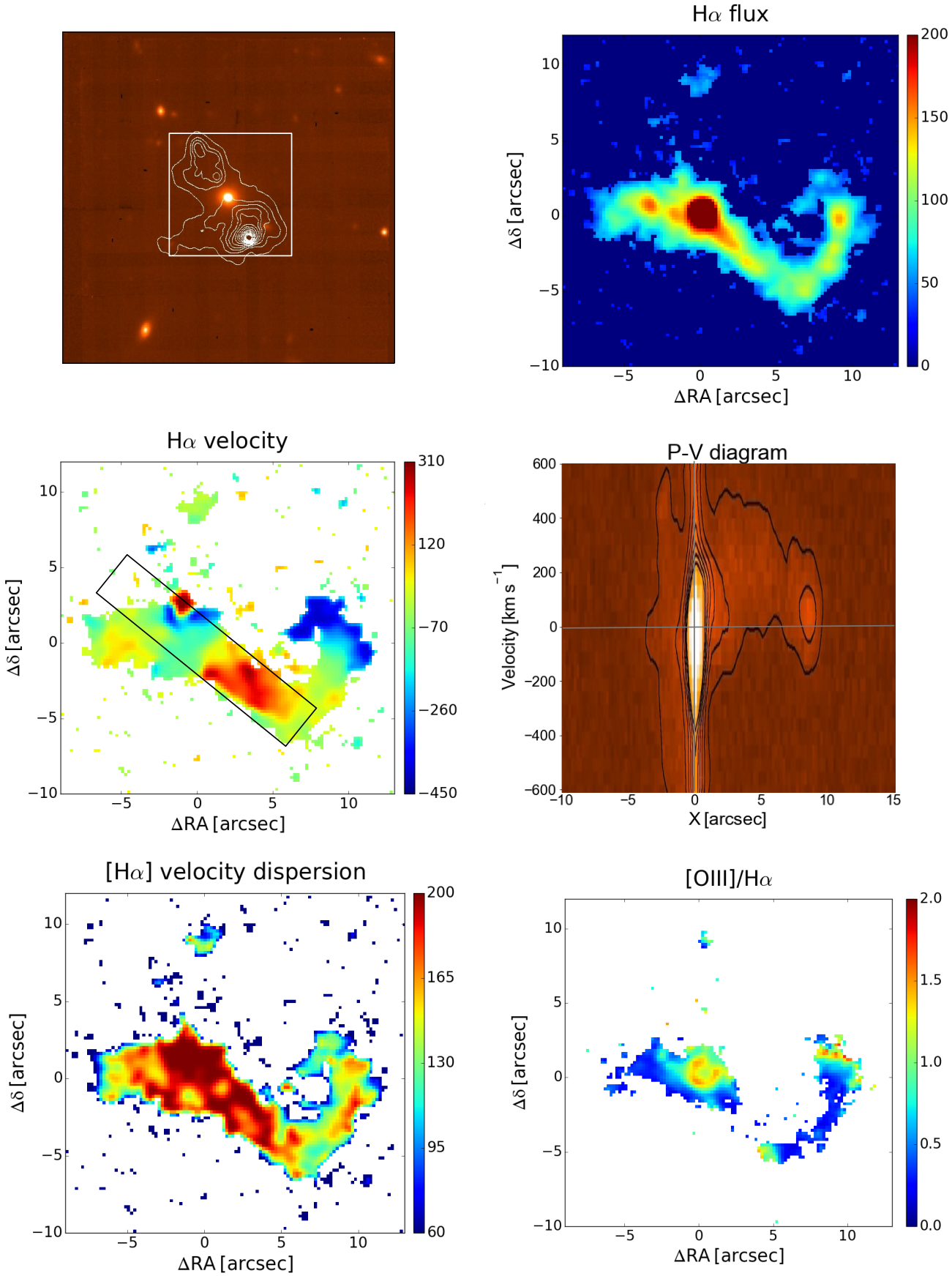

Fig. 7. 3C 063, FR II/HEG, 1″ = 2.99 kpc. *Top left*: radio contours overlaid onto the Muse optical continuum image. *Top right*: Hα emission line image extracted from the white square in the *top left panel*. *Middle*: velocity field from the Hα line and PV diagram (the synthetic slit is centered on the nucleus, has a width of 5 pixels and it is oriented at an angle of −60° from the *X* axis). *Bottom*: Hα velocity dispersion and [O III]/Hα ratio.

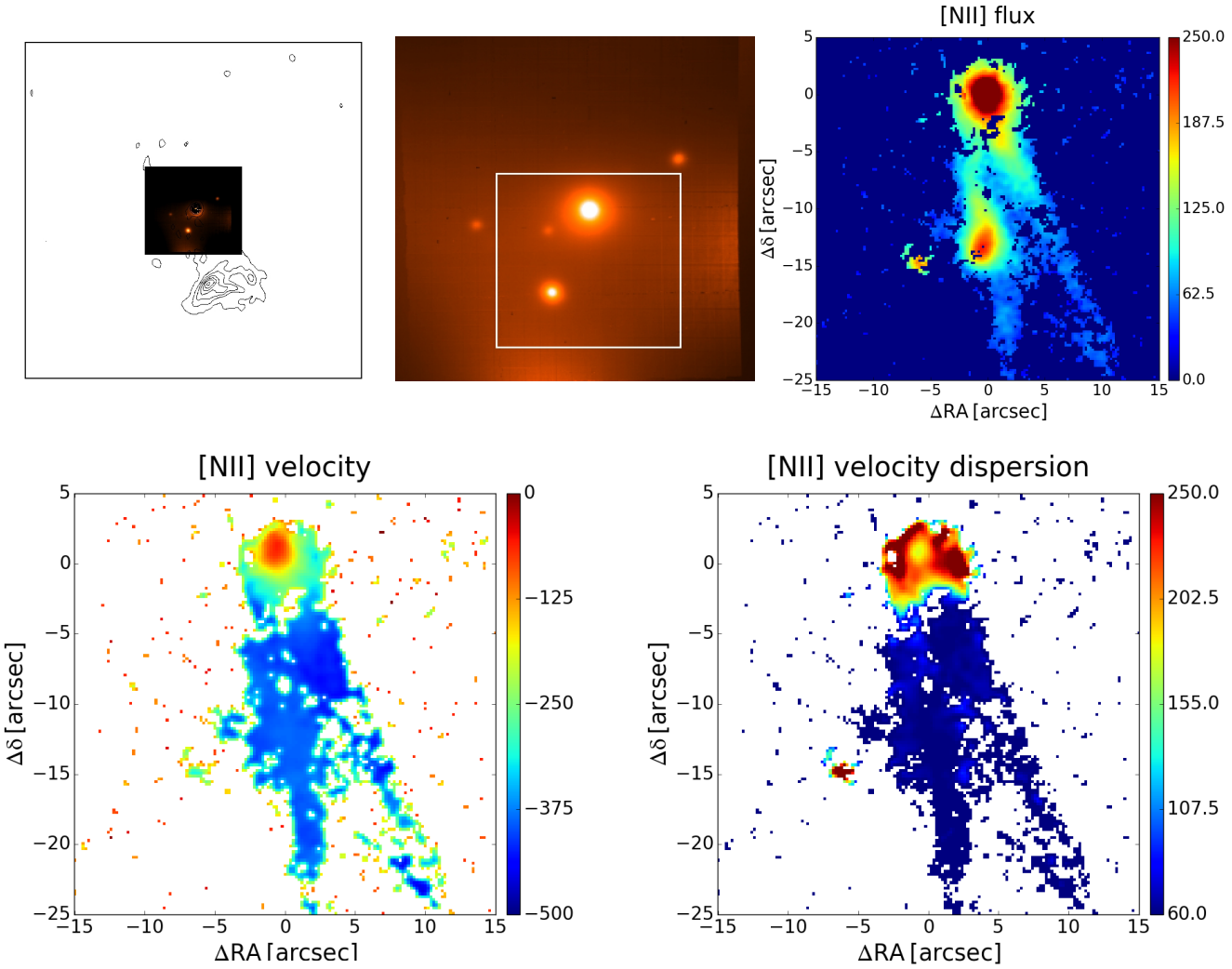

Fig. 8. 3C 318.1, complex radio morphology, no optical spectroscopic classification, FR II/HEG, 1″ = 0.90 kpc. *Top left*: radio contours overlaid onto the Muse optical continuum image. *Top center*: Muse optical continuum image. *Top right*: [N II] emission line image extracted from the white square in the *top center panel*. *Middle*: velocity field and velocity dispersion from the [N II] line.

$\sim$200 km s^{-1}, out to $\sim$6″, where it reverses. On the arc-like emission line feature the velocity smoothly decreases down to $\sim-$400 km s^{-1}. The velocity dispersion is always much larger than the instrumental width, with typical values of $\sim$200 km s^{-1} and above. The [O III]/Hα ratio decreases from the nucleus toward the more extended regions.

3C 318.1. a very peculiar source from the point of view of its radio properties, a likely relic source, with an extremely steep spectrum ($\alpha^{1.28\,\mathrm{GHz}}_{235\,\mathrm{MHz}} = 2.42$) (Giacintucci et al. 2007). The line emission, beside the bright region cospatial with the host, shows two linear plumes emerging from the center and extending toward the South, at slightly different angles, for $\sim$25 kpc. One of them terminates with a bright spot, not associated with any continuum structure. The plumes show an almost constant velocity along their whole length, at slightly different velocities: the plume pointing to South is blueshifted by $\sim$230 km s^{-1}, while that to the South-West has a larger blueshift, $\sim$280 km s^{-1}. The line dispersion is much larger on the host than on the plumes, where it is generally consistent with the MUSE spectral resolution.

3C 327. FR II/HEG, 1″ = 1.94 kpc. The line emission extends in the NE-SW direction for $\sim$18 kpc. The velocity field in the central regions is apparently ordered, with a line of node inclined with respect to the geometrical axis by $\sim$40°. The gas velocity at radii larger than $\sim$3 kpc shows a full amplitude of $\sim$600 km s^{-1}. The velocity dispersion is enhanced along the line of nodes, likely due to the unresolved velocity gradients in this region. The [O III]/Hα ratio is smaller in the north and south regions, and larger in a region approximately aligned with the radio axis, suggestive of a ionization cone.

3C 348. FR I/LEG, 1″ = 2.71 kpc. A close companion, at the same redshift, is seen at $\sim$9 kpc to the NW. This is the only FR I source showing substantially extended emission line, reaching a distance of $\sim$35 kpc on the west side. The gas is mainly in rotation in the central regions, but the kinematic axis (at PA $\sim$ 20°) is almost perpendicular to the geometrical one. Following the large scale gas filaments, the gas velocity increases steadily toward larger radii, reaching an amplitude of $\sim$400 km s^{-1}. The gas velocity dispersion in highly enhanced at the nucleus and in the region cospatial with the west radio jet.

3C 353. FR II/LEG, 1″ = 0.60 kpc. In the central region the gas is in ordered rotation with a line of node oriented at PA $\sim$ 30°. An S-shaped filament extends for $\sim$22 kpc in the north-south direction. Its velocity field is rather complex: on the

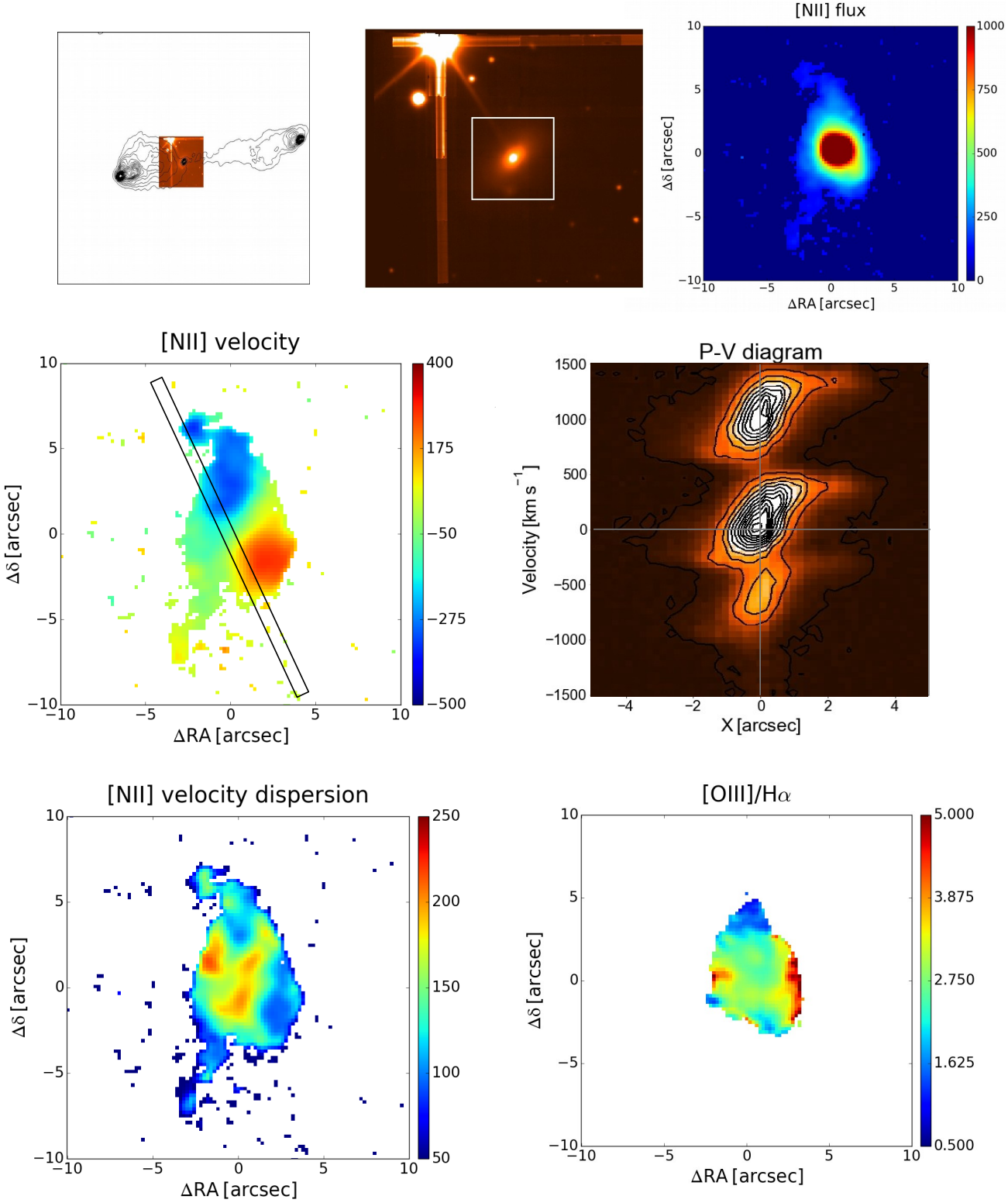

Fig. 9. 3C 327, FR II/HEG, 1″ = 1.94 kpc. *Top left*: radio contours overlaid onto the Muse optical continuum image. *Top center*: Muse optical continuum image. *Top right*: [N II] emission line image extracted from the white square in the *top center panel*. *Middle*: velocity field from the [N II] line and PV diagram (the synthetic slit is centered on the nucleus, has a width of 10 pixels and it is oriented at an angle of −52° from the *X* axis). *Bottom*: [N II] velocity dispersion and [O III]/Hα ratio.

north side the gas is initially blueshifted by ∼100 km s^{-1}, but its velocity then steadily increases at larger radii before falling back to the systemic velocity for $r > 10$ kpc. In the central ∼3 kpc both the velocity dispersion and the [N II]/Hα ratio are larger than in the regions at larger radii.

3C 386. FR II, 1″ = 0.35 kpc. Line emission is detected out to the edges of the MUSE field of view, covering a distance of at least 16 kpc. Beside the central source, it forms linear diffuse structures in the E–W direction, perpendicular to the radio lobes. Gas rotation around PA ∼ 30° is seen in the central regions.

On the west side the velocity amplitude increases steadily reaching ∼300 km s^{-1}. On the opposite side the line is also generally redshifted, but reaching lower velocities, with the two filaments showing different velocities. Lines are broader along the line of nodes which coincides with the radio axis. Our data confirm the presence of a star superposed onto the nucleus (Lynds 1971; Buttiglione et al. 2009).

3C 403. FR II/HEG, 1″ = 1.15 kpc. The ionized gas extends over ∼45 kpc forming a diffuse structure in the NE–SW direction. Most of the gas is apparently in very regular rotation with a line of nodes oriented at PA ∼ −30° with a large velocity gradient in the central ∼3 kpc, reaching an amplitude of ±300 km s^{-1}, followed by a smooth decrease at larger radii. High velocity blueshifted gas, reaching ∼800 km s^{-1} is seen on the nucleus. Similarly to what is seen in 3C 033, lines are broader in a region almost aligned with the line of nodes. The [O III]/Hα ratio is larger in the off-nuclear regions.

3C 403.1. FR II/LEG, 1″ = 1.07 kpc. The line morphology in this source is particularly complex. There is a central region extending ∼9 kpc around the host galaxy and apparently showing well ordered rotation. However, the ionized gas also forms a series of elongated structures, mainly on the E and SE direction, with compact knots joined by more diffuse emission. There are several galaxies in the MUSE field of view, but only a few emission line knots are associated with them. These extended structures, reaching a distance of ∼35 kpc, are all found at very similar velocities, being redshifted by ∼150−200 km s^{-1} with respect to the host velocity. Overall, the gas structure is reminiscent of the gas bubble seen in 3C 317. In 3C 403.1, however, there is no apparent correspondence with the location of the radio emission which extends to much larger radii, ∼230 kpc, although the available radio image is at very low spatial resolution (∼45″).

3C 424. FR II/LEG, 1″ = 2.29 kpc. The emission line structure is dominated by a bright linear feature in the EW direction which shows an overall blueshift of ∼100 km s^{-1}. More diffuse emission extends along a perpendicular axis out to ∼30 kpc with an overall redshift of ∼150 km s^{-1} on the SE side but reaching ∼450 km s^{-1} on the NW side where we also find the regions of highest velocity dispersion, up to ∼450 km s^{-1}. Generally, the nuclear regions have a higher [N II]/Hα ratio that the rest of the emission line nebula.

3C 442. FR II/LEG, 1″ = 0.53 kpc. Two compact knots, separated by ∼0.7 kpc dominate the emission line structure. They show a velocity offset of ∼130 km s^{-1} but their spectra are very similar from the point of view of the line ratios and this does not suggest, unlike the case of 3C 459 discussed below, the presence of a dual AGN. At large radii two tongues of ionized gas extends in the SW direction for ∼4 kpc, a feature reminiscent of the edges of the cavity seen in the 3C 317 (Balmaverde et al. 2018b), but the resolution of the available radio images does not allow us to perform a detail comparison between these structures. Along the same SW direction diffuse gas is detected out to a radius of ∼14 kpc, showing an almost constant velocity of ∼150 km s^{-1}. On the SW side there is another diffuse structure, apparently unrelated to the filaments pointing more to the South based on both its location and much larger blueshift (up to ∼400 km s^{-1}) not associated with any galaxy in the field.

3C 445. FR II/BLO, 1″ = 1.09 kpc. The emission line region in this source has a triangular shape, elongated in the SW direction out to a radius of ∼20 kpc. The gas velocity is roughly constant, with a redshift of ∼150 km s^{-1}. The [O III]/Hα ratio increases from the nucleus to the outer regions.

3C 456. FR II/HEG, 1″ = 3.74 kpc. The emission line region in this source is compact, confined within ∼10 kpc. Nonetheless, it clearly shows rotation around PA ∼ 45° and large velocity dispersion up to ∼350 km s^{-1}.

3C 458. FR II/HEG, 1″ = 4.38 kpc. Ionized gas is detected at a distance of more than 100 kpc. It is located in various clumps forming various elongated structures, in a general NE-SW direction. The gas velocity field is also rather complex: although there is a tendency for the gas located in the NE quadrant to be generally redshifted (and to be blue-shifted in the SW one) there are changes of speed occurring on small scale.

3C 459. FR II/BLO, 1″ = 3.58 kpc. We presented the results obtained for this source in Balmaverde et al. (2018b). We detected diffuse nuclear emission and a filamentary ionized gas structure forming a one sided triangular-shaped region extending out to ∼80 kpc. The central emission line region is dominated by two compact knots of similar surface brightness separated by 1.″2 (5.3 kpc). Based on the dramatic differences in velocity, line widths, and line ratios, we argued that we are observing a dual AGN system, formed by a radio-loud AGN and a type 2 QSO companion.

4. Ionization properties of the extended emission line regions

The integral field spectroscopic data allow us to explore the ionization properties by comparing the emission line strength in different spaxels (e.g., Singh et al. 2013), but this approach requires to have detected at least four emission lines in each spaxels. To increase the S/N, we extracted spectra from synthetic apertures as far as possible from the nuclei, but still in regions of sufficient signal to derive useful emission line measurements. We discarded the sources which are too compact to obtain off-nuclear measurements. The selected areas are marked in Fig. B.12 and listed in Table 2. They are located at a median distance of ∼13 kpc from the nucleus, but reach distances of ∼80 kpc. In Table 2 we list the line ratios for each source and derive a spectroscopic classification based on the location of each source in the diagnostic diagrams defined by (Kewley et al. 2006), see Fig. B.13.

Seven sources fall into the region populated by Seyfert/HEGs: they are all objects classified as HEGs also based on the nuclear line ratios (Buttiglione et al. 2010), see Table 2. Similarly, we find the same classification for the nucleus and for the extended region in two LEGs, namely 3C 353 and 3C 442. However, there is one HEGs, 3C 458, in which the emission line ratios measured on the extended emission correspond to a different spectroscopic type, for which we derive a LEG classification. In this case the extended emission line region is located at very large distance from the nucleus (80 kpc). The transition from high to low ionization appears to occur gradually, based on the decrease of the [O III]/Hα ratio with distance (see Fig. B.9).

Finally, there are four sources with a peculiar behavior, namely 3C 63 (a HEG), 3C 318.1 and 3C 386 (both of uncertain spectral type), and 3C 424 (a LEG): they are located in different regions of the diagnostic diagrams depending on the panel considered, an indication that we might not be observing regions in which photoionization from an active nucleus or from young stars is not the dominant process. This is reminiscent of the results found with MUSE observations by Balmaverde

Table 2. Synthetic aperture for the off-nuclear spectra and diagnostic line ratios.

Name (type)	Size	Distance (″)		(kpc)	[O III]/Hβ	[N II]/Hα	[S II]/Hα	[O I]/Hα	Type
3C 017 (BLO)	1.2	2.4 W	0.0 N	10.5	4.74	0.74	0.64	0.31	HEG
3C 018 (BLO)	2.0	3.4 W	0.6 N	13.0	16.72	1.11	0.60	0.13	HEG
3C 033 (HEG)	2.0	4.0 E	3.6 N	6.3	14.54	0.34	0.26	0.12	HEG
3C 063 (HEG)	4.0	8.6 W	1.4 S	30.1	1.18	0.30	0.52	0.22	Peculiar
3C 318.1 (–)	1.6	0.4 E	13.0 S	11.7	0.23	1.24	0.43	0.16	Peculiar
3C 327 (HEG)	2.0	0.4 E	3.8 N	8.1	11.64	1.33	0.75		HEG
3C 353 (LEG)	4.0	0.8 E	19.8 N	12.7	<1.90	0.66	0.69		LEG
3C 386 (–)	4.0	11.4 E	0.0 N	4.2	0.66	1.01	0.28		Peculiar
3C 403 (HEG)	4.0	6.8 E	6.6 N	11.3	>9.50	1.15	0.72		HEG
3C 424 (LEG)	4.0	5.8 E	6.8 S	2.4	0.77	0.68	0.58	0.18	Peculiar
3C 442 (LEG)	1.2	0.4 W	4.6 S	3.0	>0.52	3.00	1.74	0.40	LEG
3C 445 (BLO)	4.0	11.8 W	9.8 S	17.0	8.20	0.15	0.35	0.08	HEG
3C 458 (HEG)	2.0	7.8 E	11.6 N	80.2	5.60	0.58	0.99	0.53	LEG
3C 459 (BLO)	1.2	12.4 W	9.8 N	69.0	5.50	0.18	0.68		HEG

Notes. Column description: (1) source name; (2) region size (arcseconds); (3) distance from the nucleus in arcseconds and (4) kpc, (5,6, and 7) diagnostic line ratios, (8) spectroscopic type.

et al. (2018b) for 3C 317: we argued that ionization due to slow shocks (Dopita & Sutherland 1995) or collisional heating from cosmic rays (Ferland et al. 2008, 2009; Fabian et al. 2011) might be important. The general small sigma of the emission lines in these regions, ∼50−100 km s^{-1}, argues against the importance of shocks, thus favoring ionization from energetic particles.

5. Discussion

The MUSE data reveal a relationship between the radio morphology and the warm ionized gas structures. Objects belonging to the FR I and FR II classes behave differently: we did not detect extended line emission in three out of four FR I despite their lower redshift (ranging 0.018–0.073) with respect to FR II. The only exception is the FR I, 3C 348. In all the FR II observed (with the only exception of 3C 456) we observe ionized gas extending up to 20 effective radii of the host. In most cases these structures exhibit a filamentary shape, reminiscent of tidal tails (3C 327, 3C 348, 3C 353, 3C 386, 3C 403.1, 3C 442, 3C 458, and 3C 459). In some cases these filaments seem to connect the radio galaxy with a galaxy at the same redshift (e.g., 3C 403.1, 3C 018, and 3C 424), suggesting that FR II radio galaxies often inhabit a dynamic environment, as seen also by high redshift studies (Chiaberge et al. 2018). In one case (3C 063) we observe ionized gas emission around the expanding radio lobe, similarly to 3C 317 (Balmaverde et al. 2018b). No apparent difference emerges between the FR II of HEG or LEG spectral class.

Overall, we observe extended line emission structures in FR II are preferentially (but not exactly) oriented perpendicularly to the radio jets. The tendency for the radio ejection to occur along the rotation axis of gas/dust disks has been strongly debated in past, resulting in contrasting results. Heckman et al. (1985) found that in radio galaxies with radio emission larger than >100 kpc, the radio jet and the gas rotational axis are typically aligned to within a few tens of degree. We defer the detailed analysis of the velocity fields and of the relationship between radio and line emission to a forthcoming paper.

We compare our results with the study of extended optical emission-lines gas in low redshift radio galaxies, presented by Baum et al. (1988), Baum & Heckman (1989), in which they presented narrow band images of a representative sample of powerful radio galaxies. The spatial resolution of the images was ∼1.5–2″, down to a surface brightness limit in the range 10^{-17}–10^{-16} erg s^{-1} cm^{-2} arcsec^{-2}. They commonly detected extended optical-line-emitting gas and in some cases filaments of ionized gas on scales of 40–100 kpc, departing from the host galaxy. Seven MURALES objects are in common with their sample: the comparison of the contour map with MUSE images shows that, although with lower spatial resolution and sensitivity, their narrow band filter images already captures the overall morphology of the extended gaseous structures. For example, they observed the S-shaped regions of line emission in 3C 063 and around the cavity in 3C 317.

The HST images of emission lines present a rather different picture with respect to the MUSE data, in particular both Privon et al. (2008) and Baldi et al. (2019) found a general alignment between the line and radio axis. This is likely due to the fact that HST is able to resolve the innermost regions of the narrow line regions while it is not sensitive to the large scale low brightness filaments.

In many galaxies the gas shows ordered motion, usually indicative of rotation on both the galactic and the larger scale. However, several sources depart from this description, e.g. 3C 063, 3C 424, and 3C 458, while in other objects the gas velocity field is highly complex.

Baum et al. (1990) obtained long-slit optical spectra along the extended emission line features (see also Heckman et al. 1985). Inspecting the velocity curves along different position angles, they classified the emission line nebulae into rotators, calm rotators or violent rotators. Their kinematical classification corresponds generally to the morphological separation into FR I and FR II radio galaxies: rotators or violent rotators are nearly always associated with FR II HEGs, while instead the calm non rotators are preferentially of FR I or FR II LEGs type. Our MUSE data reveal that objects of these latter two classes (e.g. 3C 353) actually show rotational motions that was not spatially resolved in their data. This applies also to at least two FR Is of our sample (namely, 3C 040 and 3C 348). We thus believe the objects belonging to the "calm non rotators" show well defined rotation with data of adequate spatial resolution, like in this work.

The maps of velocity dispersion often show quasi-linear regions of high velocity dispersion: the best examples are 3C 033 and 3C 403 (but a similar feature is seen also in 3C 327, 3C 348,

3C 353, and 3C 386). In 3C 033 the velocity dispersion reaches $\sim$200 km s^{-1}, to be compared with a value of $\sim$70 km s^{-1} across the remaining of the emission line region, similar values are seen also in 3C 403. These features do not show a preferential relation with the radio axis, while they are generally perpendicular to the axis along which the emission line region is elongated. The origin of this effect is unclear. The high velocity dispersion could be due to interstellar material shocked by the expanding radio jet (Couto et al. 2017) or to higher turbulence due to the presence of strong backflow toward the inner regions produced by the expansion of the radio cavity (e.g. Cielo et al. 2017; Antonuccio-Delogu & Silk 2010).

From the point of view of the line ratios we find a variety of behaviors, with sources in which the [O III]/Hα ratio decreases with radius (e.g., 3C 018 and 3C 458) but also sources in which it increases (e.g., 3C 017 and 3C 445). In 3C 033, 3C 327, and 3C 403, the map of the emission line ratios show the pattern reminiscent of a ionization cone, in which the [O III]/Hα flux ratio map shows a biconical shape.

Our analysis of the large scale emission line regions shows that generally the spectroscopic type derived from the line ratios is consistent with the spectral classification based on the nuclear properties. In other sources, the emission line ratios are inconsistent with those produced by photo-ionization. Given the low velocities observed, leaving the possibility of cosmic rays heating or ionization due to slow shocks. This suggests that at very large distances the geometric dilution of the nuclear radiation field allows other ionization mechanism to prevail.

The spectra obtained also revealed significant departures from single Gaussian profiles for the emission lines, mostly in the nuclear regions (see, e.g., the high velocity component visible in the P–V diagram of 3C 403 reaching $\sim$800 km s^{-1}), that usually show asymmetric profiles with prominent high velocity wings. In a forthcoming paper, we will analyze in detail the line shapes, looking for the signature of outflows. In particular we will investigate the role of relativistic collimated jets in dragging outflows.

It has been suggested that LEGs and HEGs are related to a different accretion process, hot versus cold gas (Hardcastle et al. 2007; Buttiglione et al. 2010; Baum et al. 1995). We are probably witnessing a somewhat different situation: while we confirm the general paucity of ionized gas in FR Is, it is somewhat surprising that the FR II/LEGs show similar ionized gas structures to those of FR IIs/HEGs and BLOs. In fact LEGs are thought to be powered by hot accretion but we detect a large reservoir of warm, emitting line gas, similar to those found in HEGs. This seems to indicate that FR IIs of LEG and HEG type both inhabit regions characterized by a rich gaseous environment on kpc scale. However, the extended ionized tails and filaments observed by MUSE are only the portion of the gas reservoir that is ionized by AGN photoionization or shocks. The ionized gas structures revealed by MUSE are likely to be only the tip of the iceberg of a larger amount of colder (atomic and molecular) gas. Observations of the H I and CO emission lines are needed to obtain a robust estimate of the entire gas content in these sources.

From the spatially resolved diagnostic diagram, we might envisage that the spectral type of a FR II varies with time, responding to changes of the accretion rate on a timescale much shorter than its lifetime. The measurements of the line ratios on large scale and the general consistency (with the notable exception of 3C 458) with the nuclear classification (see Table 2) indicates that this does not generally occur on a timescale shorter than the light travel time from the nucleus to where these features are located, i.e., $\sim 5 \times 10^4$ years.

6. Summary and conclusions

We presented the first results of the MURALES project (MUse RAdio Loud Emission lines Snapshot) obtained from VLT/MUSE optical integral field spectroscopic observations of 20 3C sources with $z < 0.3$ observed in Period 99, i.e., between June and July 2017. All classes of radio morphology (FR I and FR II) and optical spectroscopic classification are represented with an almost equal share of LEGs (including four FR II/LEGs) and FR IIs HEGs and BLOs. The distribution of redshift and radio power are not statistically distinguishable from the entire population of 114 3C radio galaxies at $z < 0.3$. Our sub-sample is therefore well representative of the population of powerful, low redshift, radio galaxies.

In this present paper we focused on the properties of the ionized gas. One of the most interesting result which emerges is the detection of emission line regions extending up to $\sim$100 kpc. This is made possible by the unprecedented depth of the line emission images, reaching brightness levels, as low as a few 10^{-17} erg s^{-1} cm^{-2} arcsec^{-2}, an order of magnitude deeper that the previous studies of emission lines in radio galaxies, despite the rather short exposure time of 20′.

We detected emission lines in all sources. The emission line region is dominated by a compact component on a scale of a few kpc, likely the classical narrow line region. Large scale ($\sim$5−100 kpc) ionized gas is seen in all but one (3C 456) of the 15 FR II radio galaxies observed. Usually these structures appear as elongated filaments. Only one FR I (3C 348) shows extended emission lines. In some cases the MUSE field of view (1×1 arcmin square) covers the whole radio structure (e.g., 3C 017 and 3C 063), but in most cases the radio emission extends well beyond the portion of the sky covered by MUSE.

We found that the line emission structures are preferentially (but not exactly) oriented perpendicularly to the radio jets. Conversely, large scale gas structures aligned with the jets or surrounding the radio lobes (such as those found in 3C 317) are found only in one source, namely 3C 063. We are most likely observing gas structure associated with the secular fueling of the central SMBH. We defer the detailed analysis of the spatial relation between radio and line emission to a forthcoming paper.

The interaction between the AGN and the external medium is probably confined within the innermost regions, as indicated by the HST images, where most of the ionized gas is located. These regions are not properly spatially resolved by the MUSE emission line images. An analysis of the nuclear line profiles will be used elsewhere to study AGN driven outflows.

We presented also maps of emission line ratios ([O III]/Hα or [N II]/Hα), to identify regions characterized by different ionization states. Large spatial variations in line ratios are observed in most galaxies: moving outward from the nucleus we found sources with both increasing or decreasing gas excitation.

When possible, we compared the location of the nuclear and extended line emission regions into the spectroscopic diagnostic diagrams for 13 FR IIs: seven (two) sources are classified as HEGs and BLOs (LEGs) in the nuclear regions similarly show a high (low) excitation spectrum at larger distances. Conversely, in the HEG 3C 458, the spectrum at $\sim$80 kpc from the nucleus leads to a LEG classification. In the last three sources (3C 63, 3C 386, and 3C 424) we are probably observing regions in which collisional heating from cosmic rays, rather than photoionization, is the dominant process.

For most sources we were able to produce the velocity and velocity dispersion 2D maps and a position-velocity diagram extracting the velocity profile from a synthetic long-slit aperture

aligned with extended or interesting line structures. In most objects, the central gas is in ordered rotation, but it is highly complex in a significant fraction of our sample. On larger scales, we usually observed regular velocity fields, with small gradients.

The MUSE images confirm the general paucity of ionized gas in FR Is, while FR II/LEGs show ionized gas structures morphologically similar to those of FR IIs/HEGs and BLOs. This could indicate that FR IIs of both LEG and HEG type apparently inhabit regions characterized by a similar content of gas and, possibly, similar triggering/feeding mechanism. This would challenge previous suggestions that LEGs are powered by hot accretion (and HEGs by cold gas) while we detected a large reservoir of gas in both classes. To tackle the long standing issue of the triggering and of the origin of the fueling material in radio galaxies, we need to complement the information derived on the ionized component of the interstellar medium with observations able to trace also the cold gas component.

Acknowledgements. We acknowledge the anonymous referee for her/his report. Based on observations made with ESO Telescopes at the La Silla Paranal Observatory under programme ID 099.B-0137(A). The National Radio Astronomy Observatory is a facility of the National Science Foundation operated under cooperative agreement by Associated Universities, Inc. The radio images were retrieved from the NRAO VLA Archive Survey, (c) AUI/NRAO, available at http://archive.nrao.edu/nvas/. B.B. acknowledge financial contribution from the agreement ASI-INAF I/037/12/0. We acknowledge financial contribution from the agreement ASI-INAF n. 2017-14-H.O.

References

Antonuccio-Delogu, V., & Silk, J. 2010, MNRAS, 405, 1303
Bacon, R., Accardo, M., Adjali, L., et al. 2010, in SPIE Conf. Ser., Proc. SPIE, 7735, 773508
Baldi, R. D., Rodríguez Zaurín, J., Chiaberge, M., et al. 2019, ApJ, 870, 53
Baldwin, J. A., Phillips, M. M., & Terlevich, R. 1981, PASP, 93, 5
Balmaverde, B., Capetti, A., Marconi, A., & Venturi, G. 2018a, A&A, 612, A19
Balmaverde, B., Capetti, A., Marconi, A., et al. 2018b, A&A, 619, A83
Baum, S. A., & Heckman, T. 1989, ApJ, 336, 702
Baum, S. A., Heckman, T. M., Bridle, A., van Breugel, W. J. M., & Miley, G. K. 1988, ApJS, 68, 643
Baum, S. A., Heckman, T., & van Breugel, W. 1990, ApJS, 74, 389
Baum, S. A., Heckman, T. M., & van Breugel, W. 1992, ApJ, 389, 208
Baum, S. A., Zirbel, E. L., & O'Dea, C. P. 1995, ApJ, 451, 88
Bennett, C. L., Larson, D., Weiland, J. L., & Hinshaw, G. 2014, ApJ, 794, 135
Buttiglione, S., Capetti, A., Celotti, A., et al. 2009, A&A, 495, 1033
Buttiglione, S., Capetti, A., Celotti, A., et al. 2010, A&A, 509, A6
Cappellari, M. 2017, MNRAS, 466, 798
Cappellari, M., & Copin, Y. 2003, MNRAS, 342, 345
Carniani, S., Marconi, A., Maiolino, R., et al. 2016, A&A, 591, A28
Chambers, K. C., Magnier, E. A., Metcalfe, N., et al. 2016, ArXiv e-prints [arXiv:1612.05560]
Chiaberge, M., Tremblay, G. R., Capetti, A., & Norman, C. 2018, ApJ, 861, 56
Cielo, S., Antonuccio-Delogu, V., Silk, J., & Romeo, A. D. 2017, MNRAS, 467, 4526
Couto, G. S., Storchi-Bergmann, T., & Schnorr-Müller, A. 2017, MNRAS, 469, 1573
Cresci, G., & Maiolino, R. 2018, Nat. Astron., 2, 179
Dopita, M. A., & Sutherland, R. S. 1995, ApJ, 455, 468
Fabian, A. C. 2012, ARA&A, 50, 455
Fabian, A. C., Sanders, J. S., Williams, R. J. R., et al. 2011, MNRAS, 417, 172
Fanaroff, B. L., & Riley, J. M. 1974, MNRAS, 167, 31P
Ferland, G. J., Fabian, A. C., Hatch, N. A., et al. 2008, MNRAS, 386, L72
Ferland, G. J., Fabian, A. C., Hatch, N. A., et al. 2009, MNRAS, 392, 1475
Finlez, C., Nagar, N. M., Storchi-Bergmann, T., et al. 2018, MNRAS, 479, 3892
Gaspari, M., Temi, P., & Brighenti, F. 2017, MNRAS, 466, 677
Giacintucci, S., Venturi, T., Murgia, M., et al. 2007, A&A, 476, 99
Gitti, M., Brighenti, F., & McNamara, B. R. 2012, Adv. Astron., 2012, 950641
Hardcastle, M. J., Evans, D. A., & Croston, J. H. 2007, MNRAS, 376, 1849
Heckman, T. M., Illingworth, G. D., Miley, G. K., & van Breugel, W. J. M. 1985, ApJ, 299, 41
Hine, R. G., & Longair, M. S. 1979, MNRAS, 188, 111
Kewley, L. J., Groves, B., Kauffmann, G., & Heckman, T. 2006, MNRAS, 372, 961
Lynds, R. 1971, ApJ, 168, L87+
McCarthy, P. J., Spinrad, H., & van Breugel, W. 1995, ApJS, 99, 27
McDonald, M., Veilleux, S., Rupke, D. S. N., & Mushotzky, R. 2010, ApJ, 721, 1262
McNamara, B. R., & Nulsen, P. E. J. 2007, ARA&A, 45, 117
Privon, G. C., O'Dea, C. P., Baum, S. A., et al. 2008, ApJS, 175, 423
Russell, H. R., McNamara, B. R., Fabian, A. C., et al. 2019, MNRAS, 490, 3025
Singh, R., van de Ven, G., Jahnke, K., et al. 2013, A&A, 558, A43
Spinrad, H., Marr, J., Aguilar, L., & Djorgovski, S. 1985, PASP, 97, 932
Tremmel, M., Quinn, T. R., Ricarte, A., et al. 2019, MNRAS, 483, 3336
Veilleux, S., & Osterbrock, D. E. 1987, ApJS, 63, 295
Voit, G. M., Bryan, G. L., O'Shea, B. W., & Donahue, M. 2015, ApJ, 808, L30
Wylezalek, D., & Zakamska, N. L. 2016, MNRAS, 461, 3724

Appendix A: Nuclear and off-nuclear spectra of selected sources

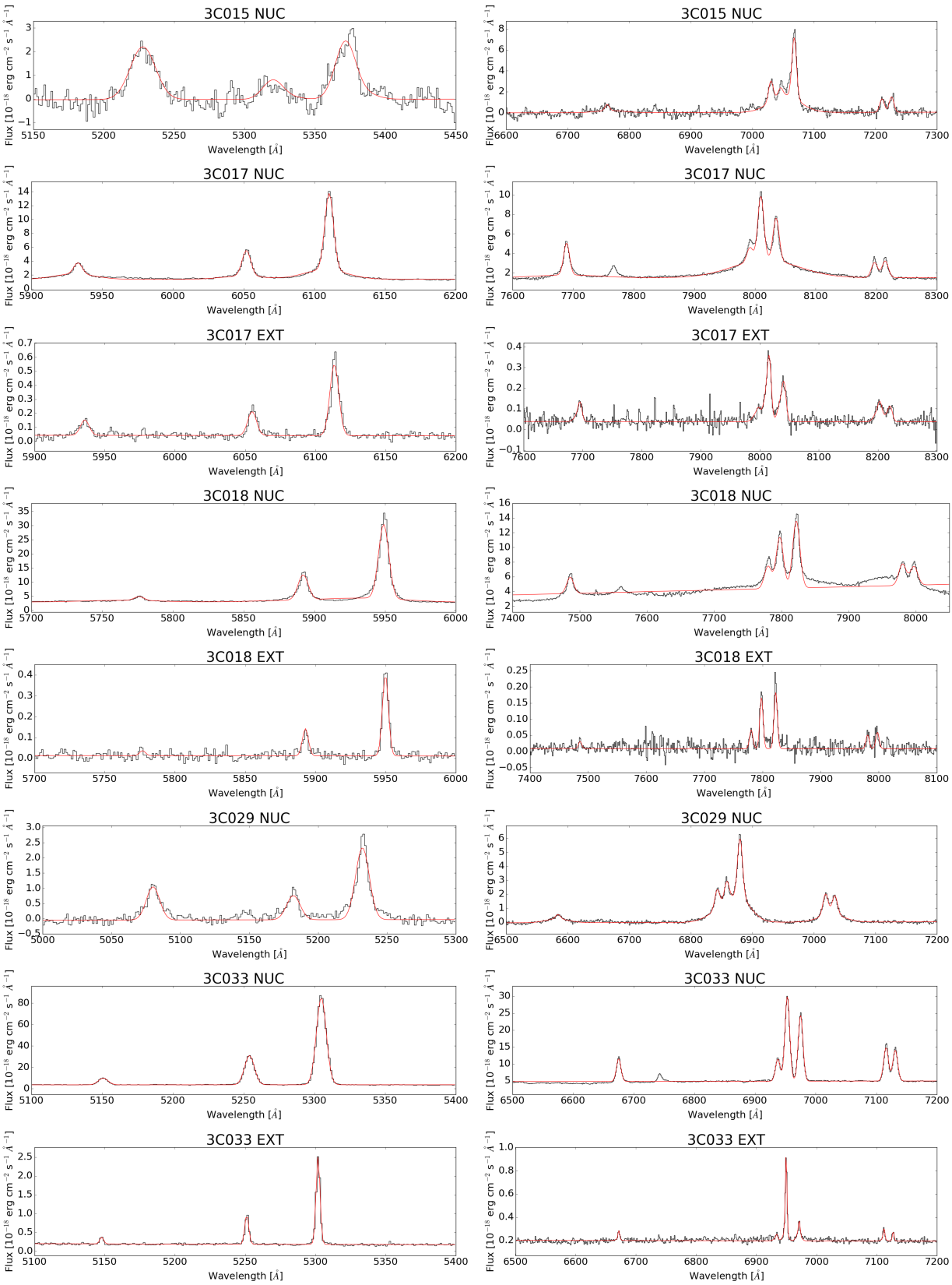

Fig. A.1. Blue (*left panel*) and red (*right panel*) portion of the nuclear spectrum for all sources; for the 14 sources discussed in Sect. 4, we also show the off-nuclear spectra extracted from the region marked in Fig. B.12.

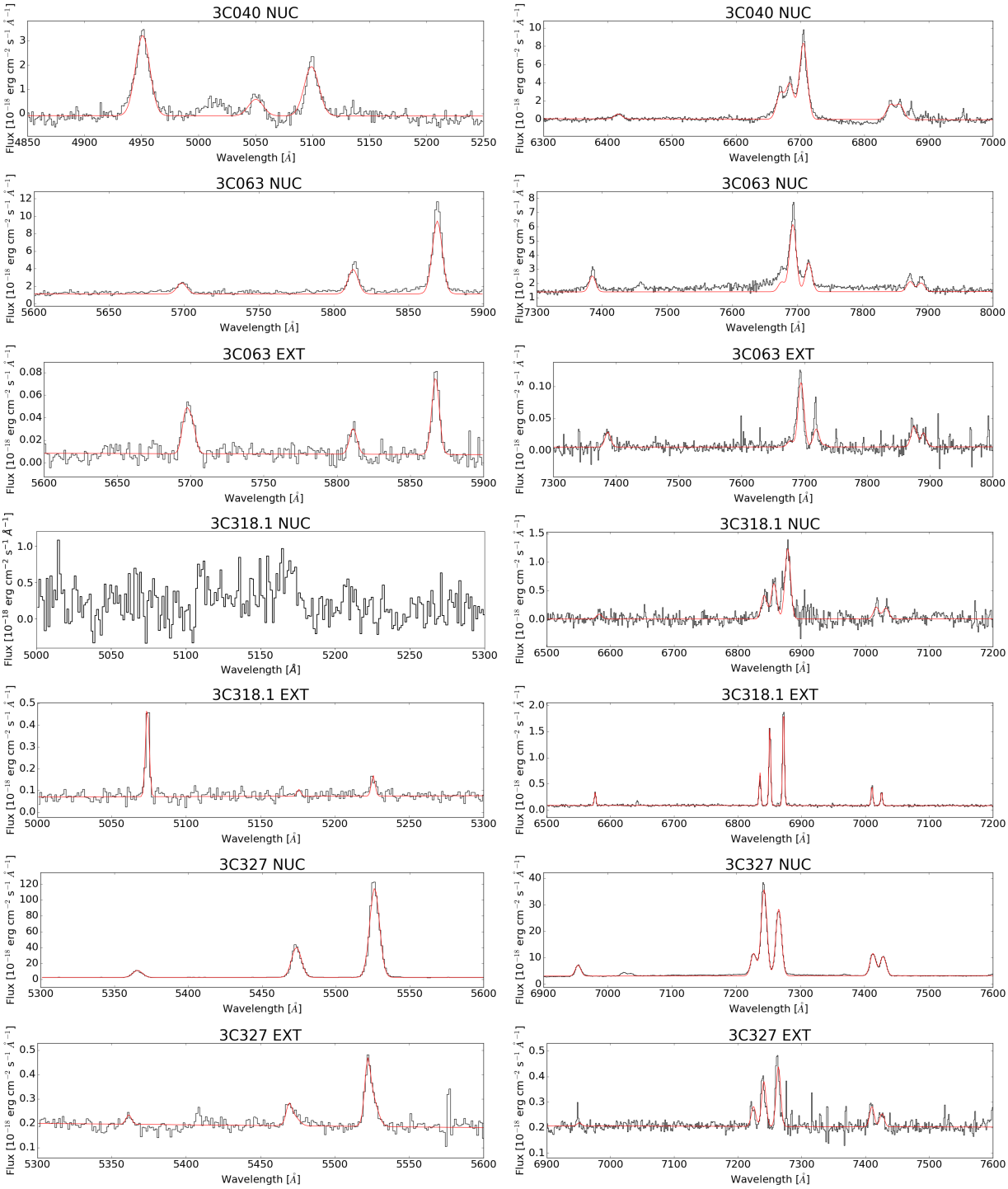

Fig. A.1. continued.

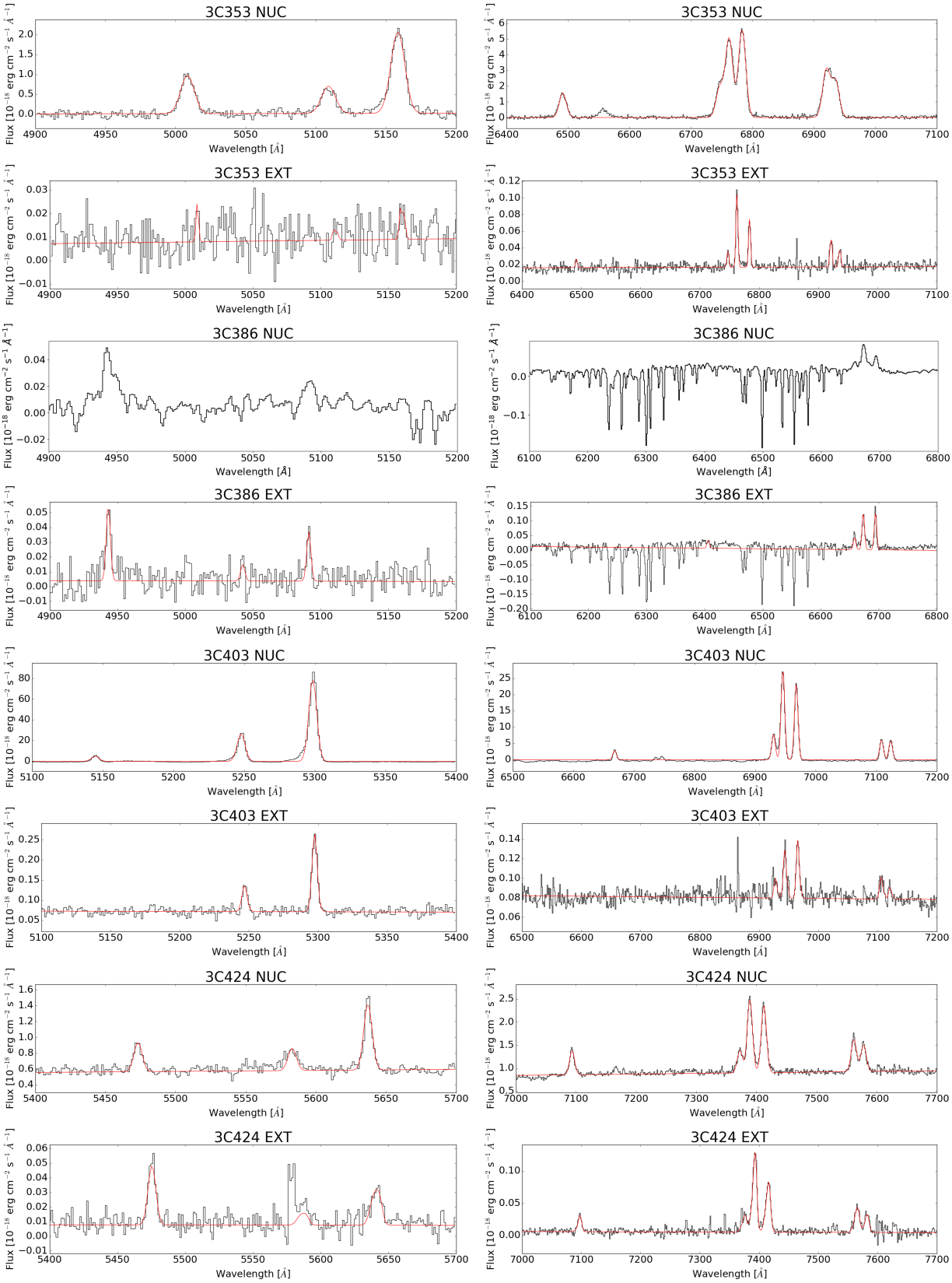

Fig. A.1. continued.

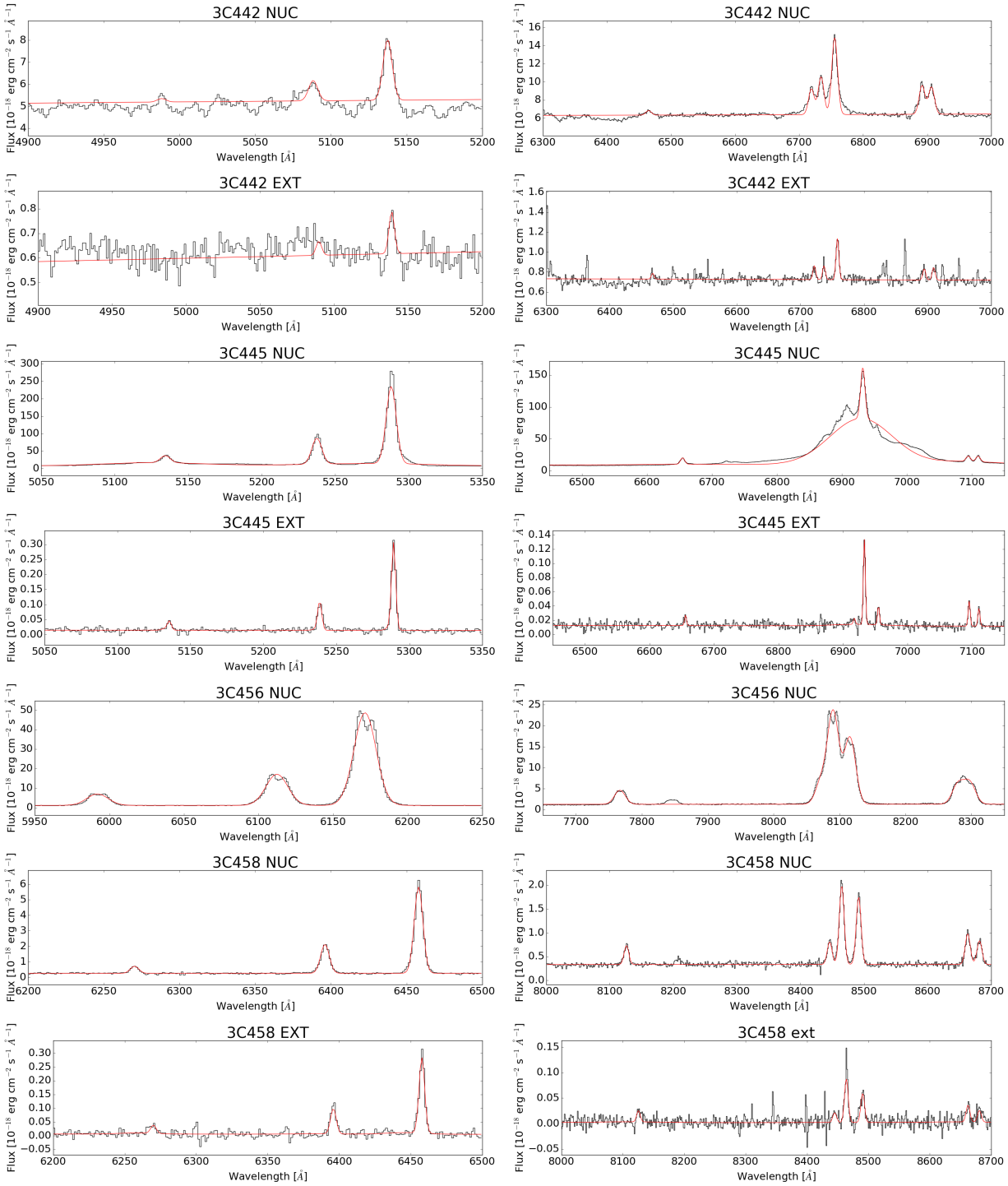

Fig. A.1. continued.

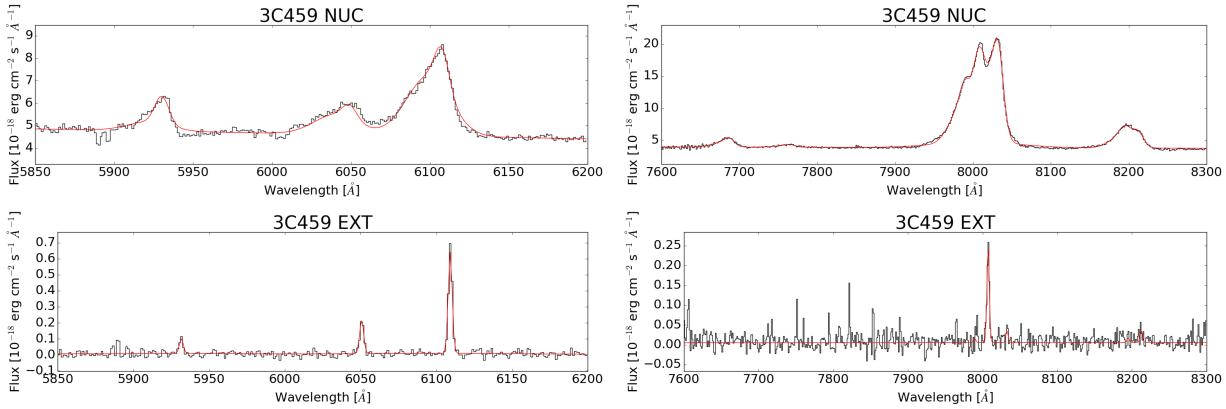

Fig. A.1. continued.

Appendix B: Additional figures

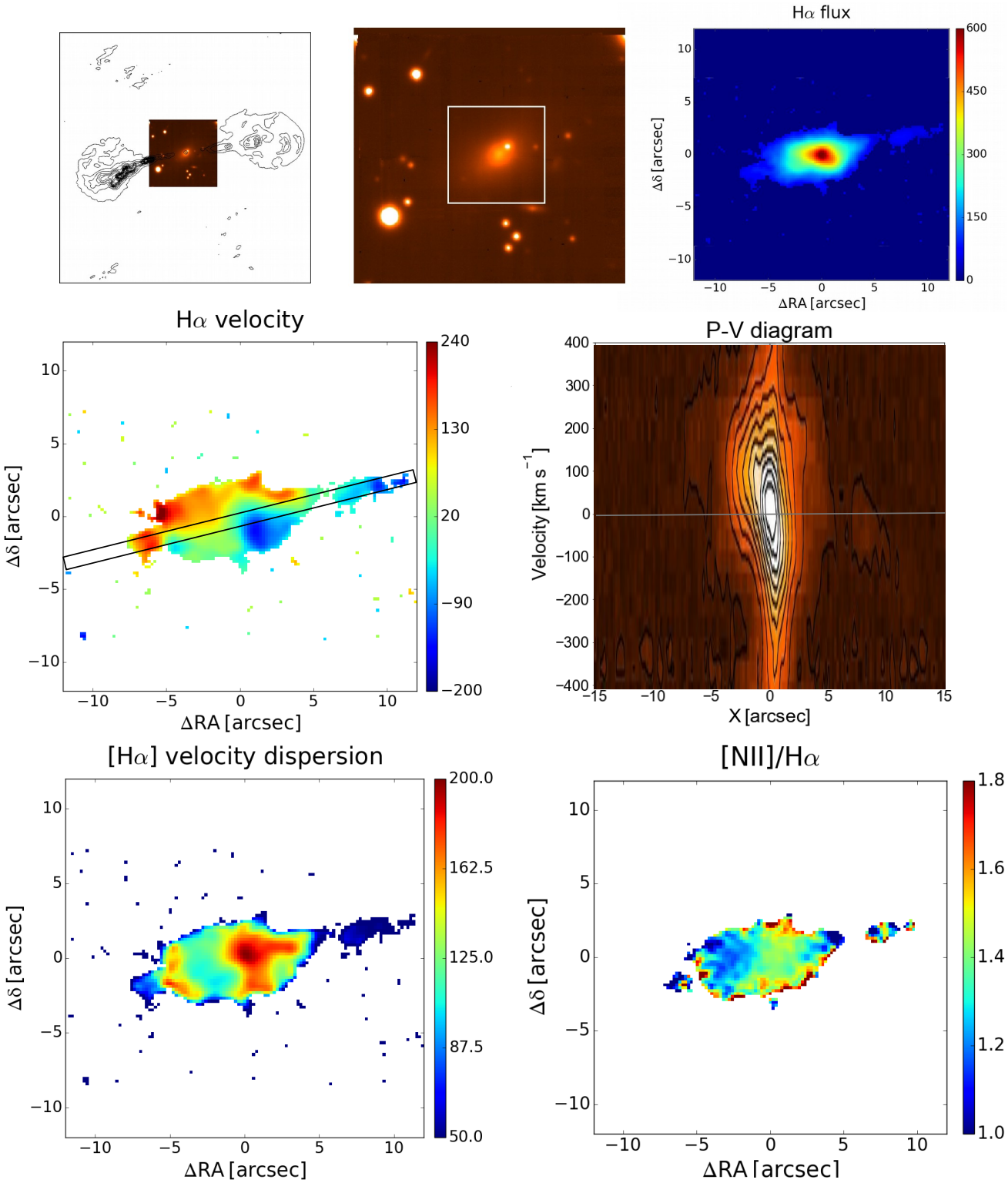

Fig. B.1. 3C 348, FR I/ELEG, 1″ = 2.71 kpc. *Top left*: radio contours overlaid onto the Muse optical continuum image. *Top center*: Muse optical continuum image. *Top right*: Hα emission line image extracted from the white square in the top center panel. *Middle*: velocity field from the Hα line and PV diagram (the synthetic slit is centered on the nucleus, has a width of 10 pixels and it is oriented at an angle of 14° from the *X* axis). *Bottom*: Hα velocity dispersion and [N II]/Hα ratio.

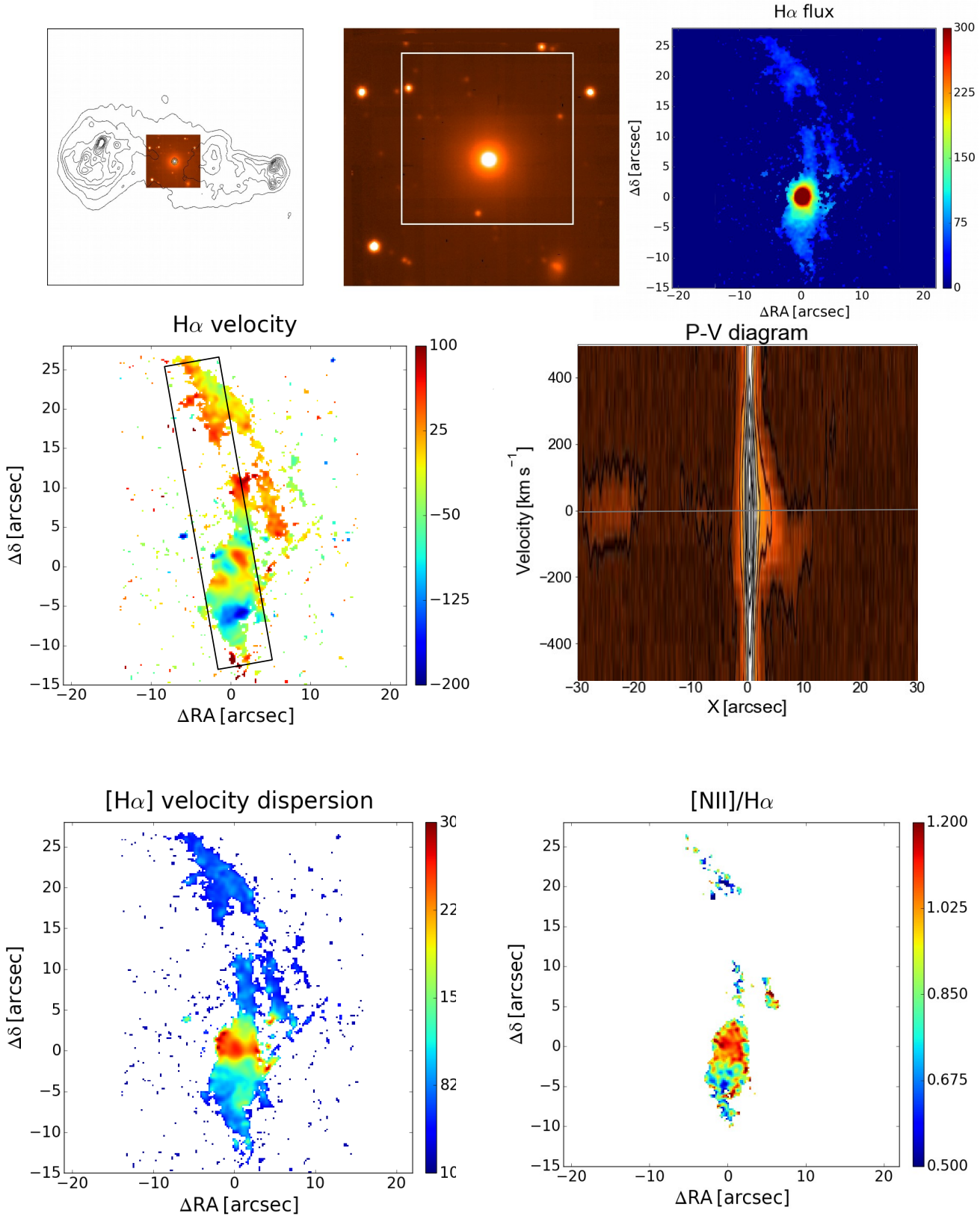

Fig. B.2. 3C 353, FR II/LEG, $1'' = 0.60$ kpc. *Top left*: radio contours overlaid onto the Muse optical continuum image. *Top center*: Muse optical continuum image. *Top right*: Hα emission line image extracted from the white square in the top center panel. *Middle*: velocity field from the Hα line and PV diagram (the synthetic slit is centered on the nucleus, has a width of 30 pixels and it is oriented at an angle of $-80°$ from the X axis). *Bottom*: Hα velocity dispersion and [N II]/Hα ratio.

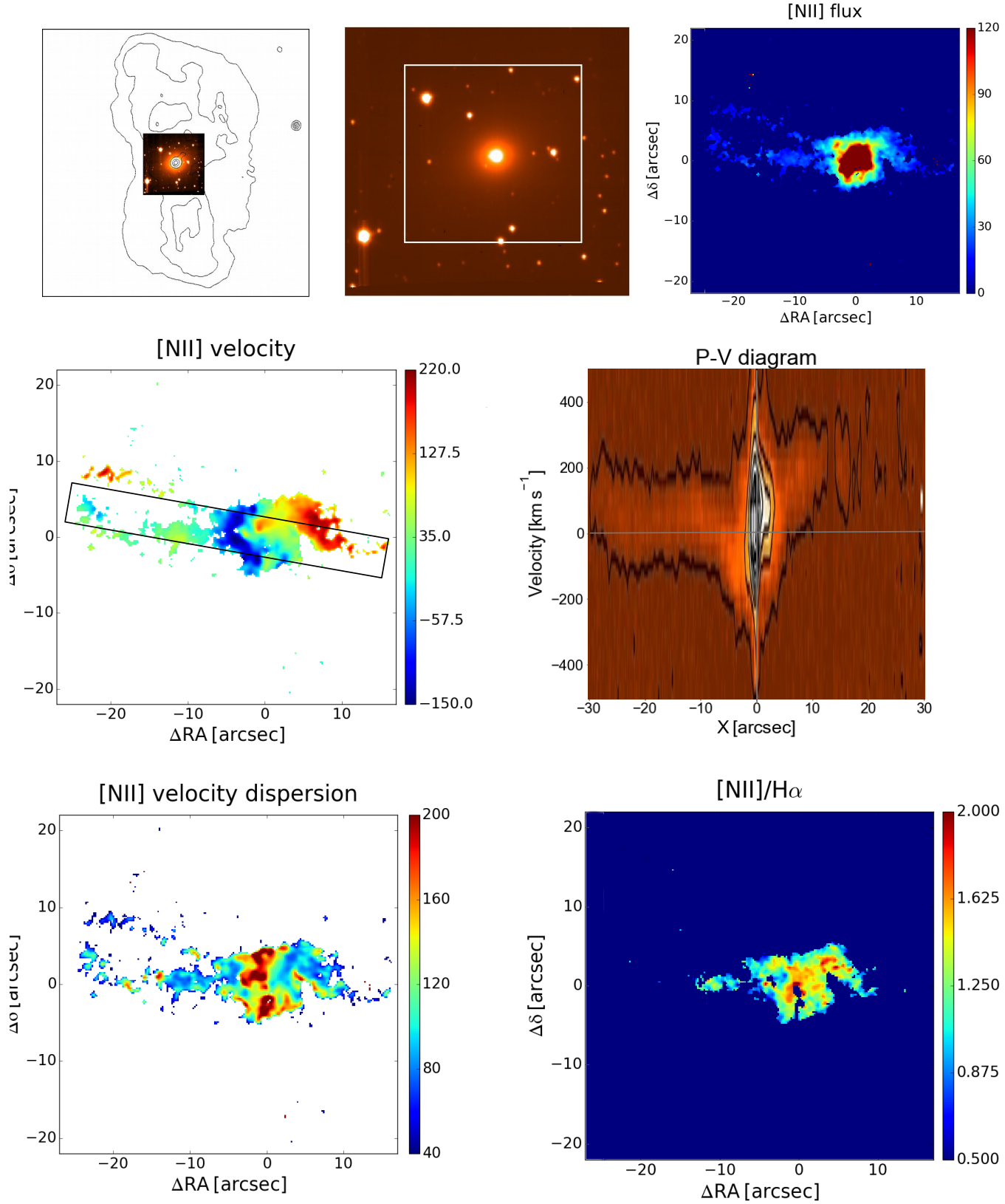

Fig. B.3. 3C 386, FR II, 1″ = 0.35 kpc. *Top left*: radio contours overlaid onto the Muse optical continuum image. *Top center*: Muse optical continuum image. *Top right*: [N II] emission line image extracted from the white square in the top center panel. *Middle*: velocity field from the [N II] line and position velocity diagram extracted from the synthetic slit shown overlaid onto the velocity field (the boxy region is centered on the nucleus, has a width of 30 pixels and it is oriented at an angle of −10° measured from the *X* axis). *Bottom*: [N II] velocity dispersion and [N II]/Hα ratio.

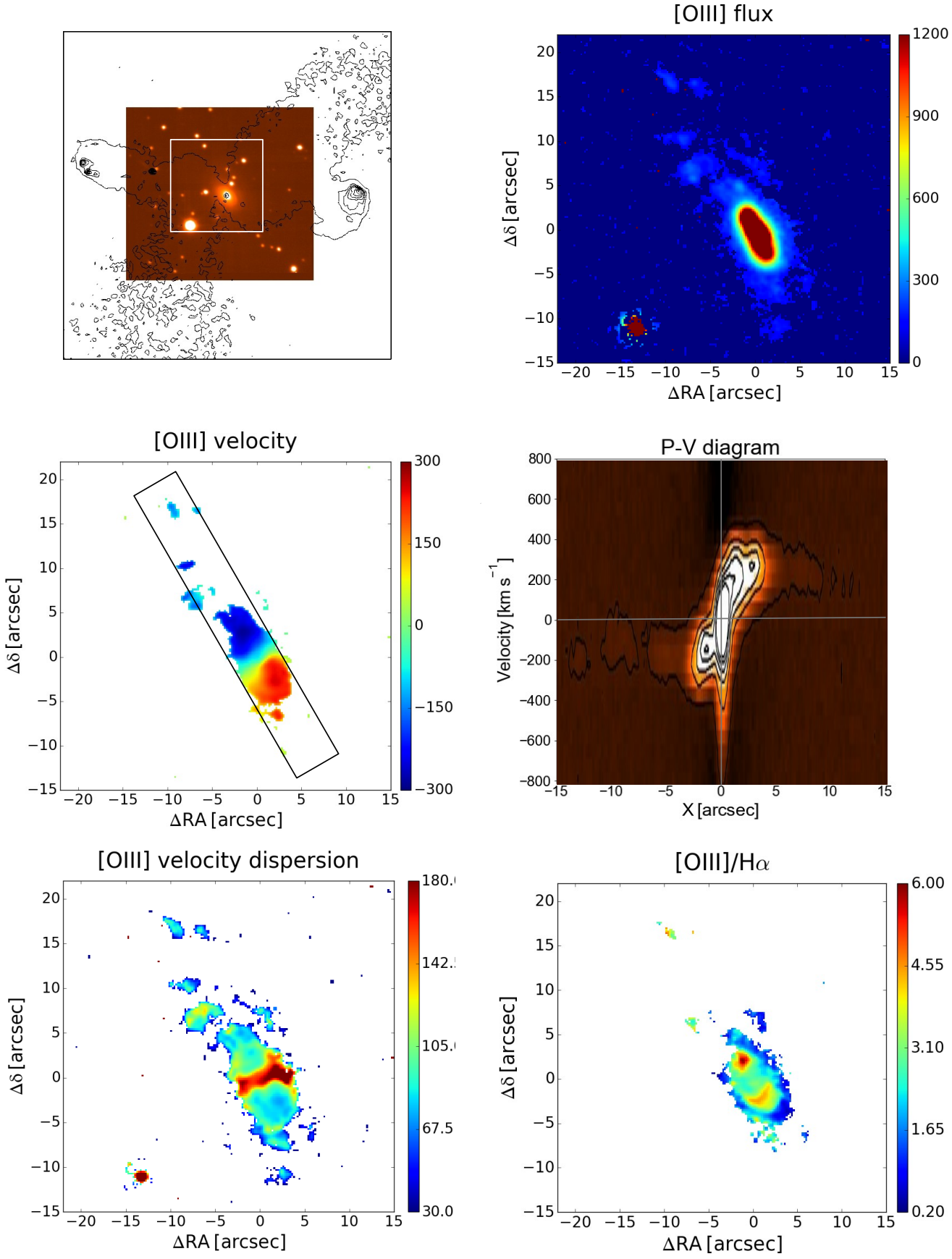

Fig. B.4. 3C 403, FR II/HEG, 1″ = 1.15 kpc. *Top left*: radio contours overlaid onto the Muse optical continuum image. *Top right*: [O III] emission line image extracted from the white square in the top left panel. *Middle*: velocity field from the [O III] line and PV diagram (the synthetic slit is centered on the nucleus, has a width of 30 pixels and it is oriented at an angle of −60° from the *X* axis). *Bottom*: [O III] velocity dispersion and [O III]/Hα ratio.

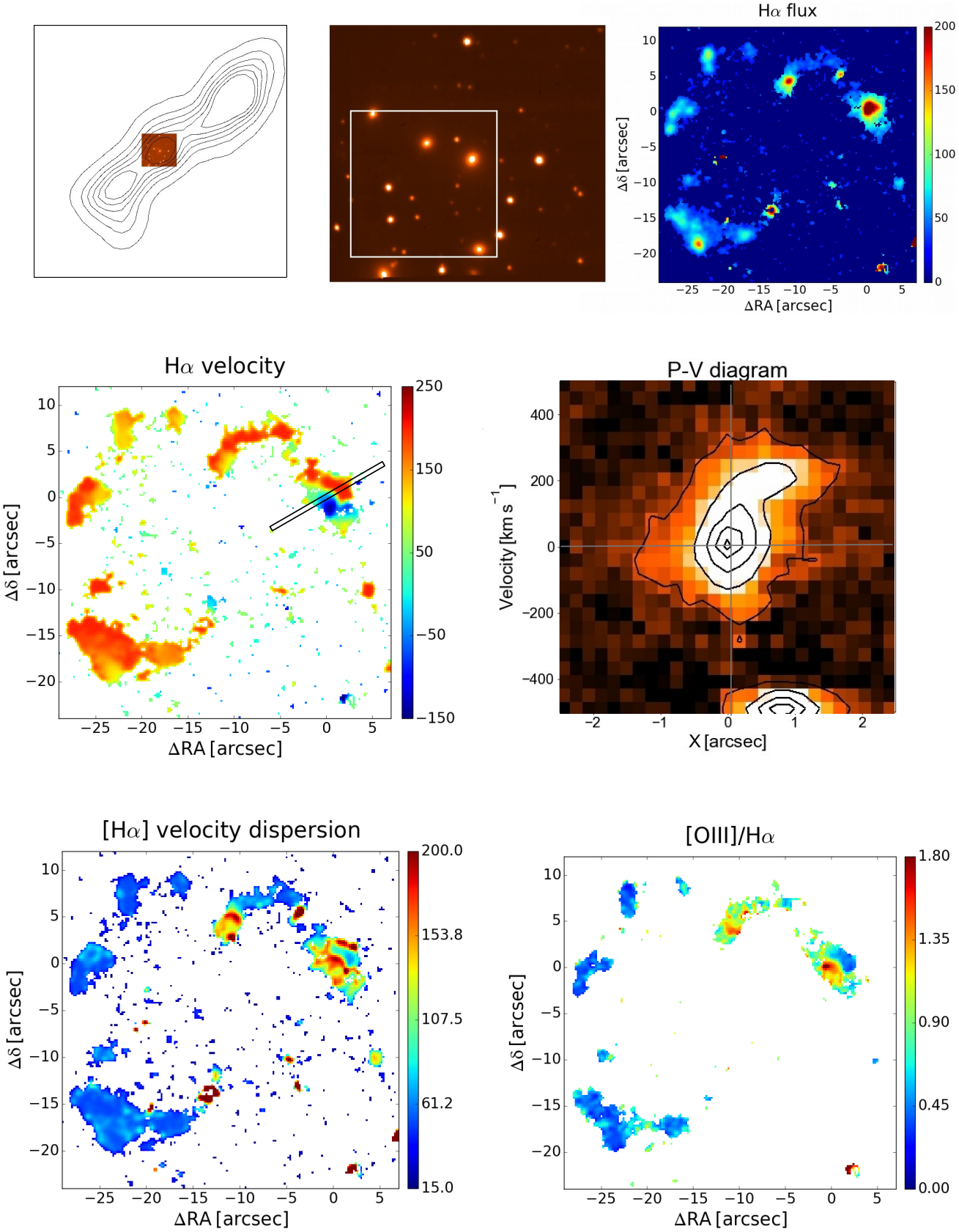

Fig. B.5. 3C 403.1, FR II/LEG, 1″ = 1.07 kpc. *Top left*: radio contours overlaid onto the Muse optical continuum image. *Top center*: Muse optical continuum image. *Top right*: Hα emission line image extracted from the white square in the top center panel. *Middle*: velocity field from the Hα line and PV diagram (the synthetic slit is centered on the nucleus, has a width of 5 pixels and it is oriented at an angle of 60° from the *X* axis). *Bottom*: Hα velocity dispersion and [O III]/Hα ratio.

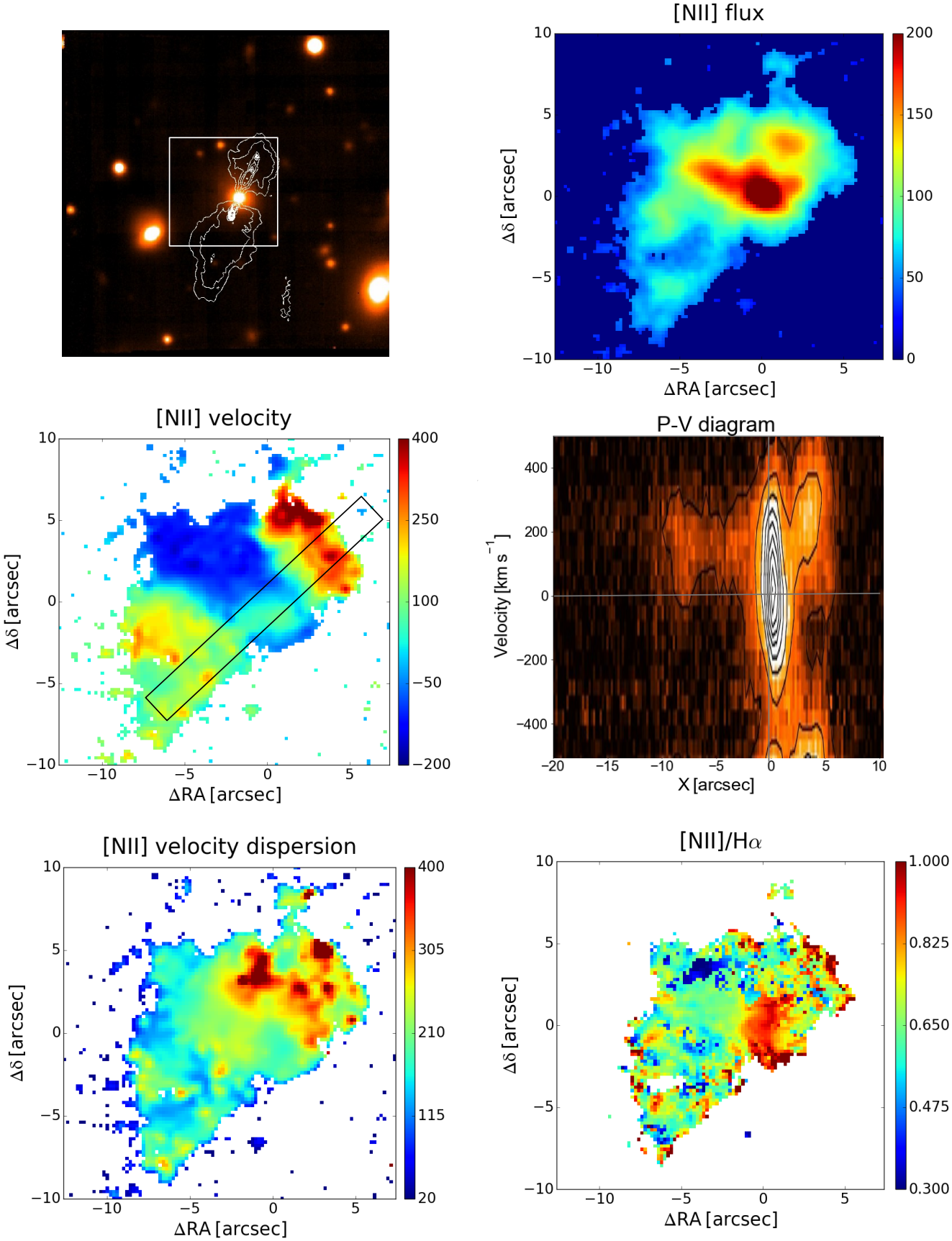

Fig. B.6. 3C 424, FR II/LEG, 1″ = 2.29 kpc. *Top left*: radio contours overlaid onto the Muse optical continuum image. *Top right*: [N II] emission line image extracted from the white square in the top left panel. *Middle*: velocity field from the [N II] line and PV diagram (the synthetic slit is centered on the nucleus, has a width of 10 pixels and it is oriented at an angle of 47° from the *X* axis). *Bottom*: [N II] velocity dispersion and [N II]/Hα ratio.

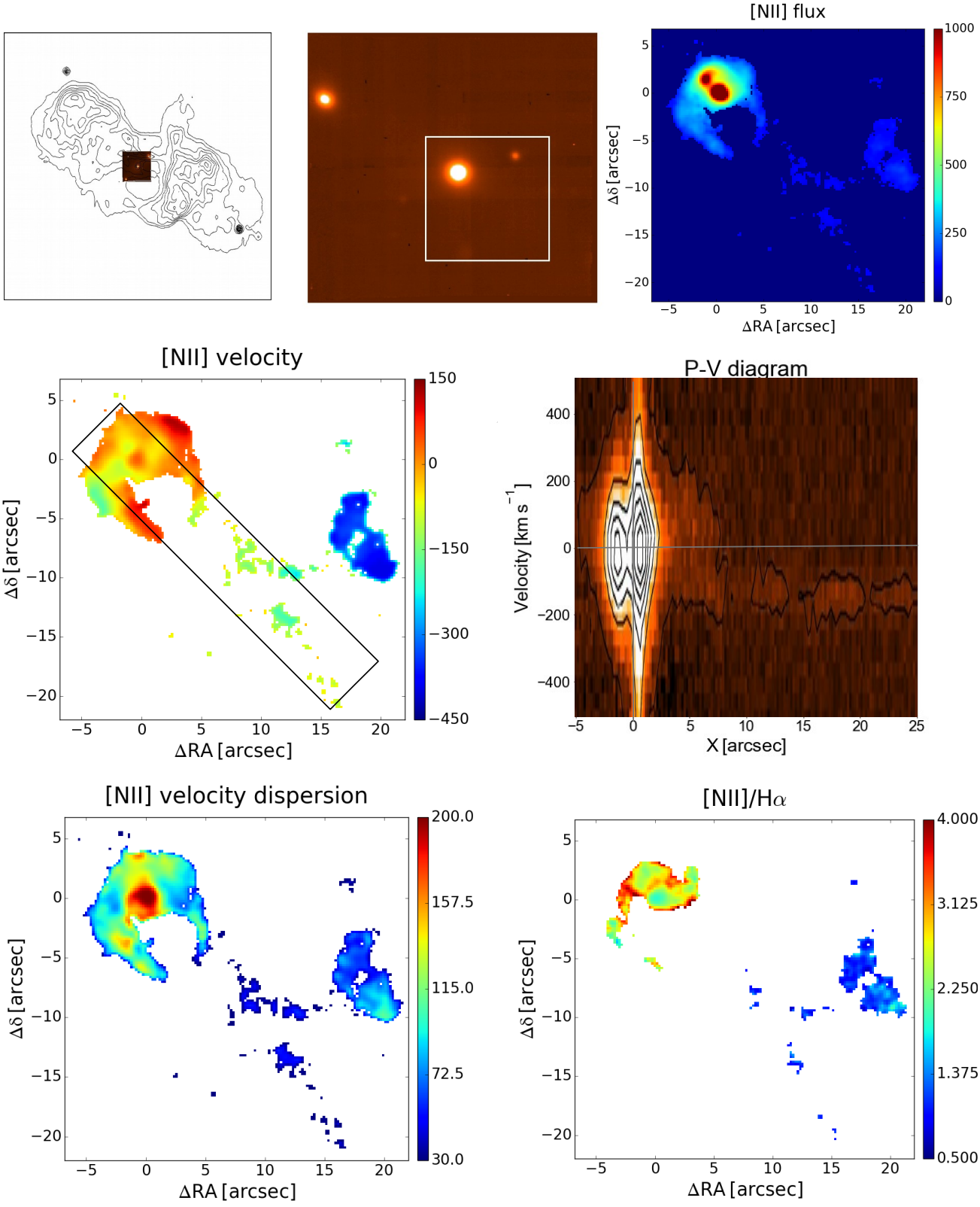

Fig. B.7. 3C 442, FR II/LEG, 1″ = 0.53 kpc. *Top left*: radio contours overlaid onto the Muse optical continuum image. *Top center*: Muse optical continuum image. *Top right*: [N II] emission line image extracted from the white square in the top center panel. *Middle*: velocity field from the [N II] line and PV diagram (the synthetic slit is centered on the nucleus, has a width of 30 pixels and it is oriented at an angle of −60° from the *X* axis). *Bottom*: [N II] velocity dispersion and [N II]/Hα ratio.

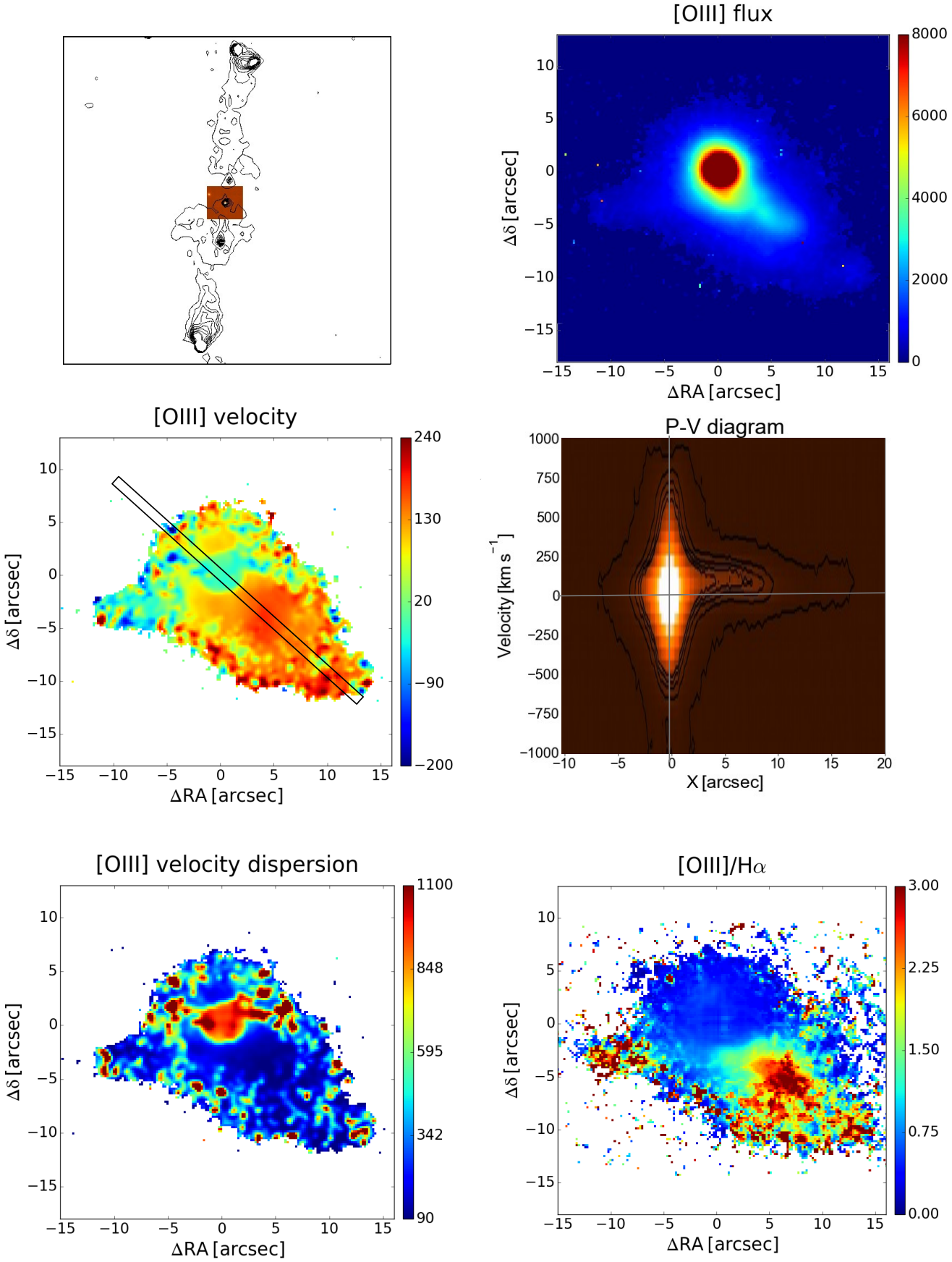

Fig. B.8. 3C 445, FR II/BLO, 1″ = 1.09 kpc. *Top left*: radio contours overlaid onto the Muse optical continuum image. *Top right*: [O III] emission line image extracted from the white square in the top left panel. *Middle*: velocity field from the [O III] line and PV diagram (the synthetic slit is centered on the nucleus, has a width of 10 pixels and it is oriented at an angle of −42° from the *X* axis). *Bottom*: [O III] velocity dispersion and [O III]/Hα ratio.

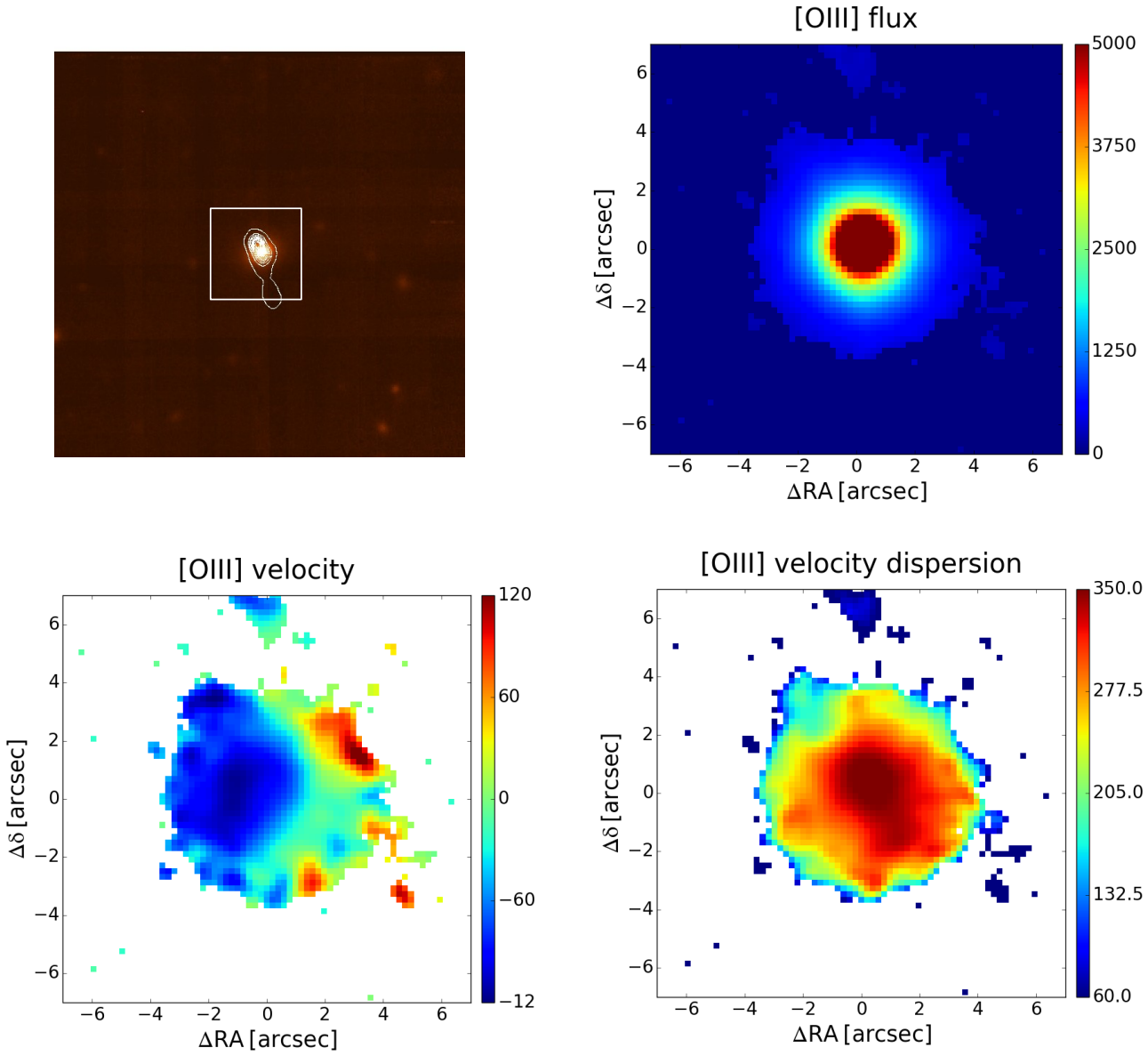

Fig. B.9. 3C 456, FR II/HEG, 1″ = 3.74 kpc. *Top left*: radio contours overlaid onto the Muse optical continuum image. *Top right*: [O III] emission line image extracted from the white square in the top left panel. *Bottom*: velocity field from the [O III] line and velocity dispersion.

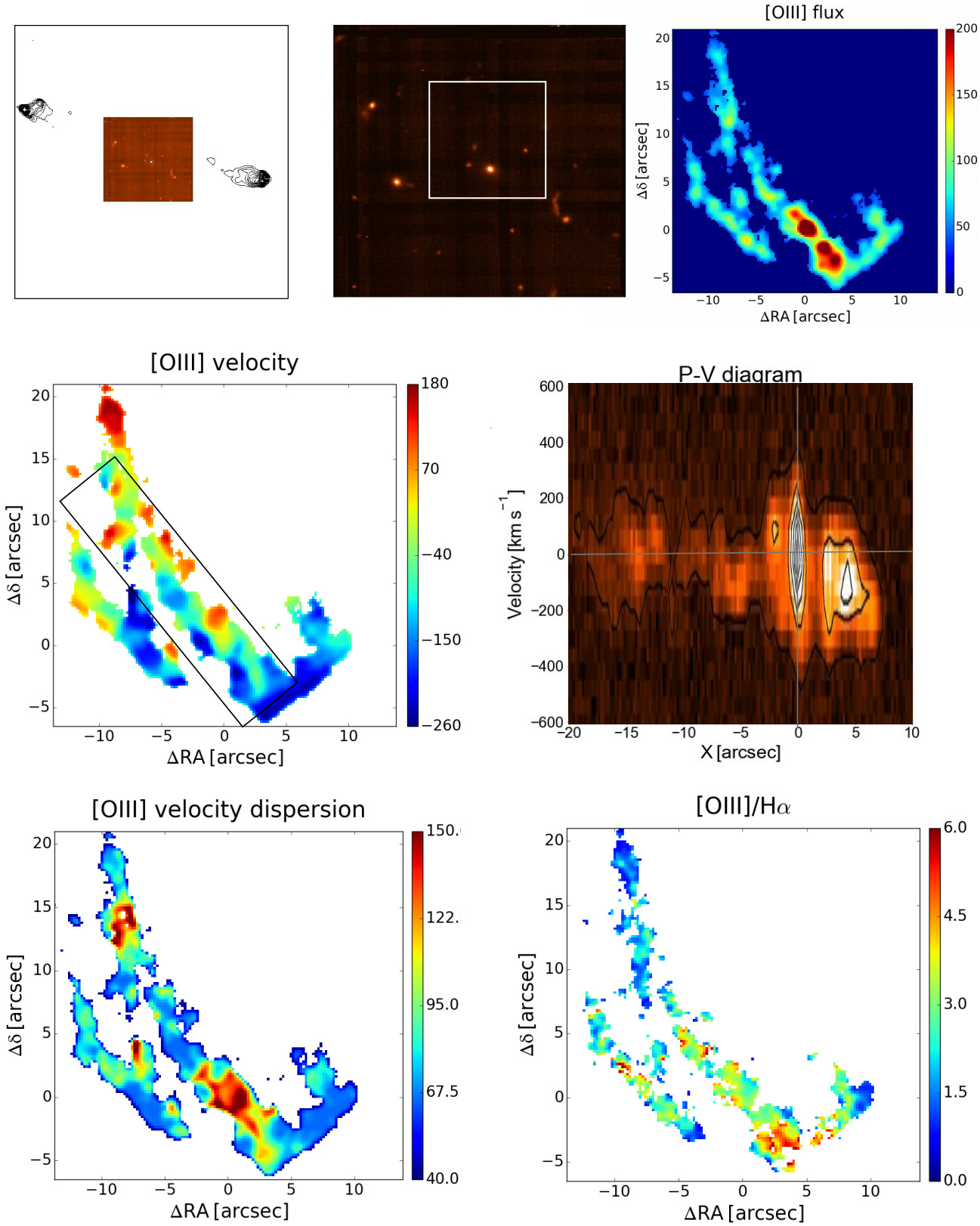

Fig. B.10. 3C 458, FR II/HEG, 1″ = 4.38 kpc. *Top left*: radio contours overlaid onto the Muse optical continuum image. *Top center*: Muse optical continuum image. *Top right*: [O III] emission line image extracted from the white square in the top center panel. *Middle*: velocity field from the [O III] line and PV diagram (the synthetic slit is centered on the nucleus, has a width of 30 pixels and it is oriented at an angle of −51° from the *X* axis). *Bottom*: [O III] velocity dispersion and [O III]/Hα ratio.

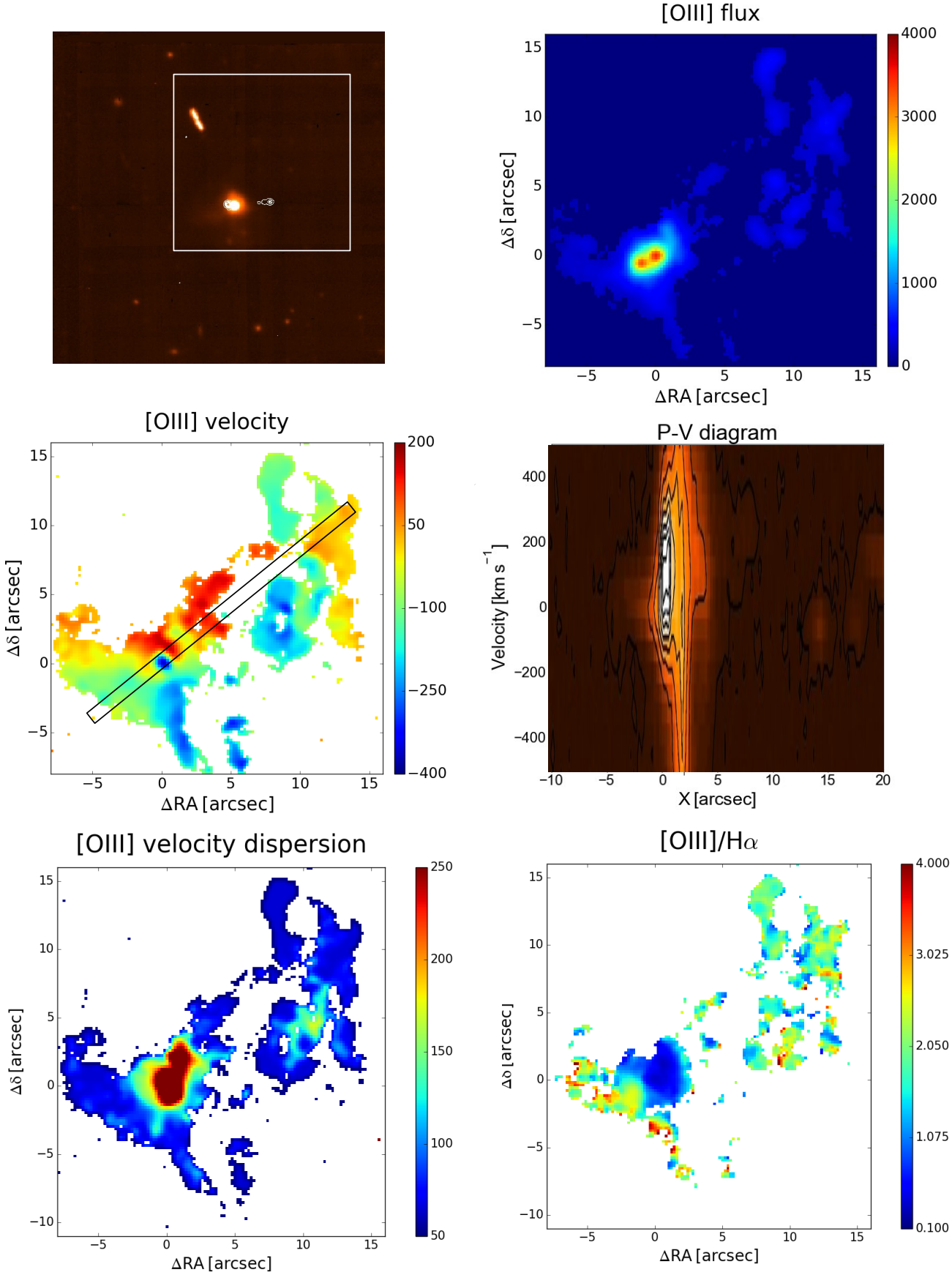

Fig. B.11. 3C 459, FR II/BLO, 1″ = 3.58 kpc. *Top left*: radio contours overlaid onto the Muse optical continuum image. *Top right*: [O III] emission line image extracted from the white square in the top left panel. *Middle*: velocity field from the [O III] line and PV diagram (the synthetic slit is centered on the nucleus, has a width of 10 pixels and it is oriented at an angle of 35° from the *X* axis). *Bottom*: [O III] velocity dispersion and [O III]/Hα ratio.

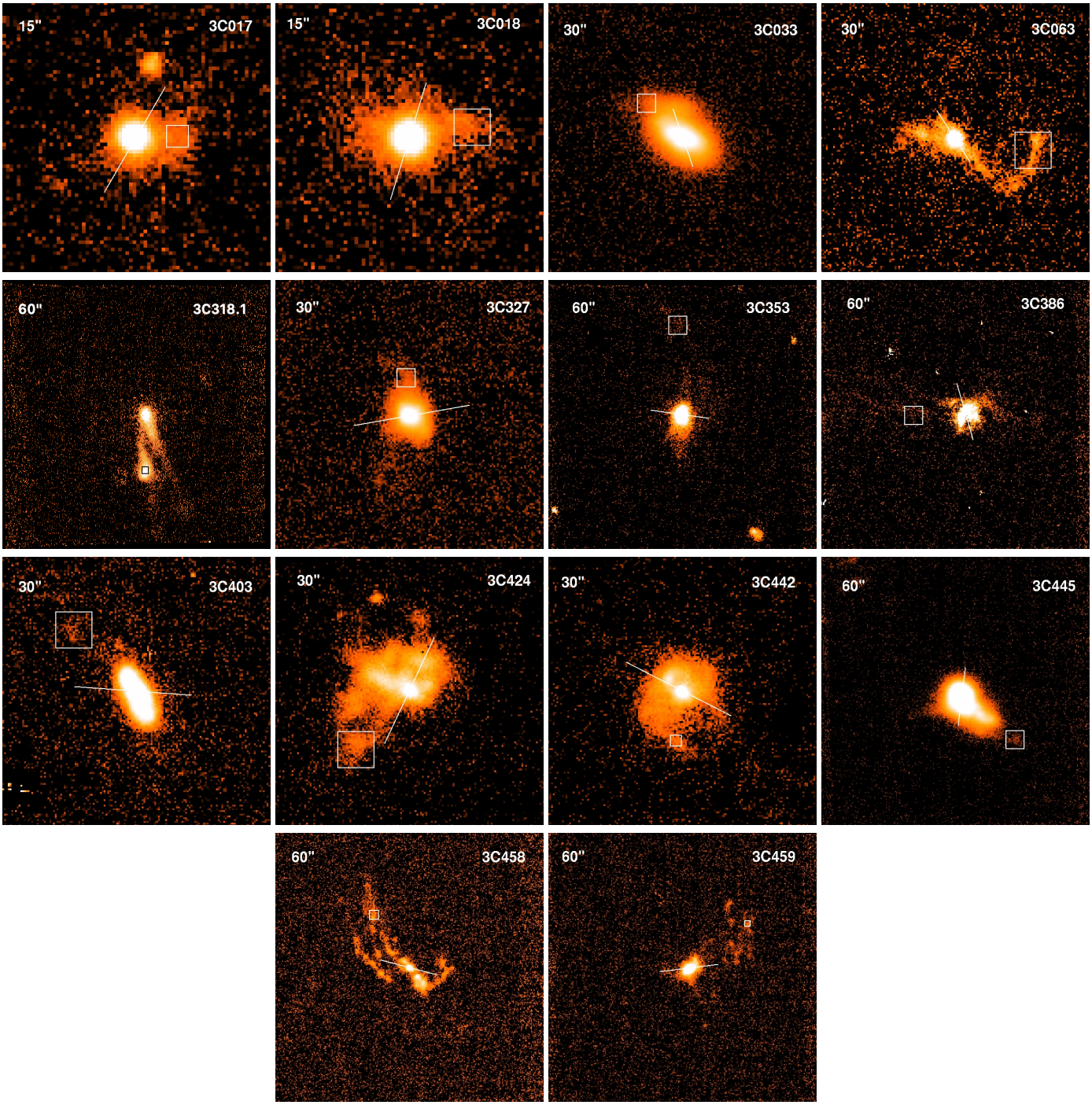

Fig. B.12. Emission line images (in logarithmic scale) of the 14 radio galaxies observed in MURALES with extended emission lines. The fields of view are indicated in the upper left corner of each image. The white segments are parallel to the radio axes, the with boxes mark the synthetic aperture from which we extracted the off-nuclear spectra.

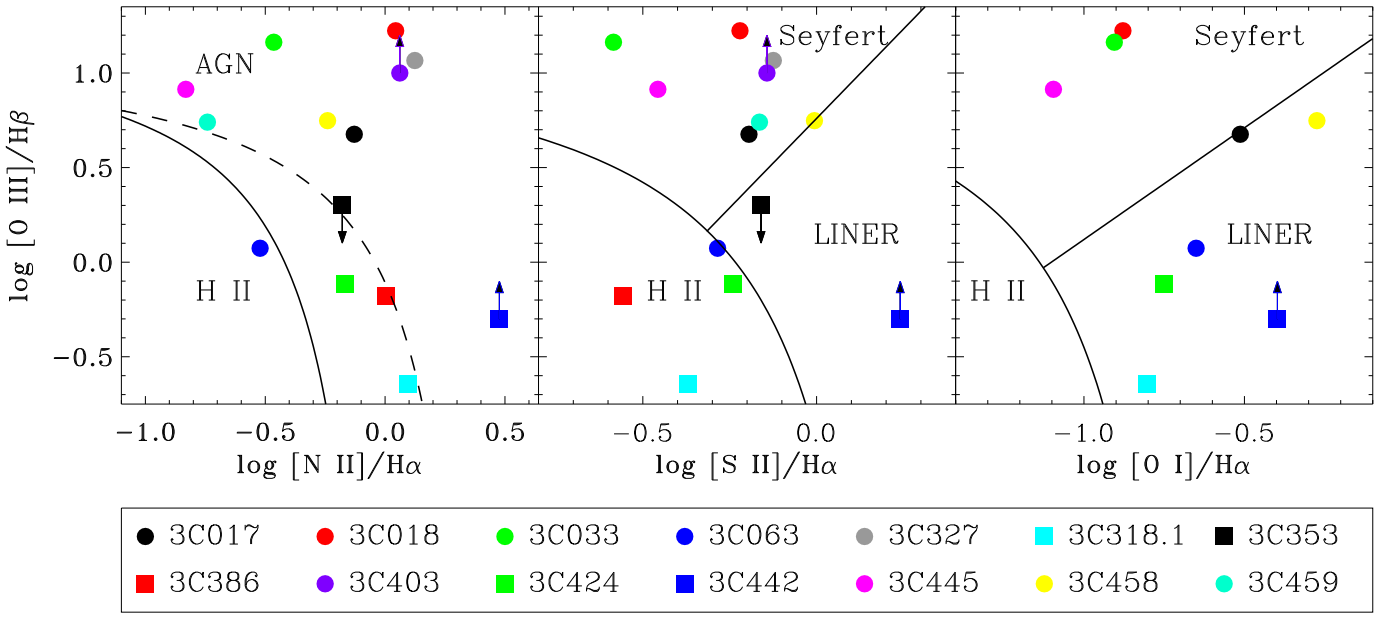

Fig. B.13. Location of the 13 FR II radio galaxies with extended line emission in the spectroscopic diagnostic diagrams. Circles (squares) correspond to source classified as HEGs (LEGs or unclassified) based on their nuclear emission line ratios (Buttiglione et al. 2010). The solid lines separate star-forming galaxies, LINERs, and Seyferts (Kewley et al. 2006).